Department of Physics and Astronomy
Heidelberg University

Bachelor Thesis in Physics
submitted by

Felix Korbinian Waldherr

born in Nürnberg (Germany)

2022

ALICE TRD electron trigger performance in pp collisions at $\sqrt{s} = 13$ TeV

This Bachelor Thesis has been carried out by Felix Korbinian Waldherr at the
Physikalisches Institut in Heidelberg
under the supervision of
Priv. Doz. Dr. Yvonne Pachmayer

Abstract

This thesis presents first results of the ALICE Transition Radiation Detector (TRD) electron trigger performance in proton-proton collisions at a center-of-mass energy of $\sqrt{s} = 13$ TeV recorded during the LHC Run 2. For the analysis, electrons were selected using the particle identification capabilities of the ALICE Time Projection Chamber (TPC). The residual hadron contamination was estimated via a fit procedure and statistically subtracted. The electron trigger efficiency of the TRD is then given as the ratio of electron candidates in the minimum bias sample that fulfill in addition the TRD trigger conditions to the electron candidates in the minimum bias sample. The trigger efficiency is studied differentially as a function of the transverse momentum p_{T}, time, the mean gain and the location within the TRD detector setup for electrons and positrons. The determined trigger efficiencies are then compared with Monte Carlo simulations and corresponding results from proton-lead collisions recorded in 2016.

Zusammenfassung

Diese Arbeit präsentiert erste Ergebnisse der Elektronentriggerleistung des ALICE Transition Radiation Detector (TRD) bei Proton-Proton-Kollisionen bei einer Schwerpunktsenergie von $\sqrt{s} = 13$ TeV, die während des LHC Run 2 aufgezeichnet wurden. Für die Analyse wurden Elektronen unter Verwendung der Teilchenidentifikationsfähigkeiten der ALICE-Zeitprojektionskammer (TPC) ausgewählt. Die restliche Hadron-Kontamination wurde über ein Fit-Verfahren abgeschätzt und statistisch subtrahiert. Die Elektronen-Trigger-Effizienz des TRD wird dann als das Verhältnis von Elektronen-Kandidaten im Minimum Bias Datensatz, die zusätzlich die TRD-Trigger-Bedingungen erfüllen, zu den Elektronen-Kandidaten im Minimum Bias Datensatz angegeben. Die Triggereffizienz wird differentiell als Funktion des Transversalimpulses p_{T}, der Zeit, des mittleren Gains und des Ortes innerhalb des TRD-Detektoraufbaus für Elektronen und Positronen untersucht. Die ermittelten Triggereffizienzen werden dann mit Monte-Carlo-Simulationen und entsprechenden Ergebnissen aus Proton-Blei-Kollisionen aus dem Jahr 2016 verglichen.

Contents

1 Introduction and Theoretical Background **1**
- 1.1 Motivation . . . 1
- 1.2 The Standard Model . . . 1
- 1.3 Particle detection . . . 2
- 1.4 Outline of thesis . . . 4

2 Detectors **5**
- 2.1 The ALICE experiment . . . 5
- 2.2 Transition Radiation Detector . . . 7
- 2.3 Time Projection Chamber . . . 9

3 Data Sample **10**
- 3.1 Event selection . . . 10
- 3.2 Track selection . . . 10
- 3.3 Monte Carlo sample . . . 11
- 3.4 TRD trigger conditions . . . 11
- 3.5 V0 data sample . . . 12

4 Trigger efficiency analysis **13**
- 4.1 Estimation of the hadron contamination . . . 14
  - 4.1.1 Comparison with modified data sets . . . 19
- 4.2 Runwise efficiency . . . 20
- 4.3 Differential analysis of the efficiency . . . 21

5 Results and Comparison **24**
- 5.1 Final TRD trigger performance . . . 24
- 5.2 Comparison with the TRD trigger in p-Pb collisions . . . 25

6 Conclusion and Outlook **28**

A Additional figures **30**
- A.1 Trigger observables . . . 30
- A.2 Hadron rejection cut method . . . 32
- A.3 Hardware status of supermodules . . . 33
- A.4 Runwise analysis . . . 33
- A.5 Additional efficiency plots . . . 35

B Runlist **36**

Bibliography **40**

1 Introduction and Theoretical Background

1.1 Motivation

A **L**arge **I**on **C**ollider **E**xperiment (ALICE) [3] at the **L**arge **H**adron **C**ollider (LHC) at CERN was built to study the properties of the quark-gluon plasma (QGP), a high-density deconfined state of strongly interacting matter created in ultra-relativistic Pb-Pb collisions. In order to study the properties of the QGP, it is necessary to measure electrons which result as decay products of sensitive probes, such as open heavy-flavour decays or decays of quarkonia, e.g Ψ and J/ψ. As reference, corresponding measurements have to be carried out in p-p and p-Pb collisions. Therefore, an excellent electron identification is needed. Furthermore, the rarity of the studied probes requires an enhancement of the probe signal with triggers, such that there is sufficient statistics for physics analyses. The ALICE **T**ransition **R**adiation **D**etector (TRD) [11] is able to fulfill these tasks. Thus, it is important to differentially study the ALICE TRD electron trigger efficiency and its dependencies on external influences that can cause deviations from the expected efficiency.

1.2 The Standard Model

In order to discuss the electron trigger efficiency of the ALICE Transition Radiation Detector (TRD) derived in this thesis, one has to understand the fundamental interactions between particles and matter, i.e. detector material. This necessitates an introduction to the Standard Model (SM) of particle physics [7]. The SM remains one of the most successful theories in physics. It provides a profound description of all fundamental particles and the interactions between them.

The SM differentiates between two types of fundamental particles: the fermions and the bosons. While fermions are the basic building blocks of matter, the bosons are responsible for the interactions between the particles. The nomenclature of these particles results from their spin properties. While fermions carry a spin of $\frac{n}{2}$, bosons are particles with a spin of n, if $n \in \mathbb{Z}$. The Higgs Boson is a particle with spin 0. The structure of the SM is shown in 1.1.

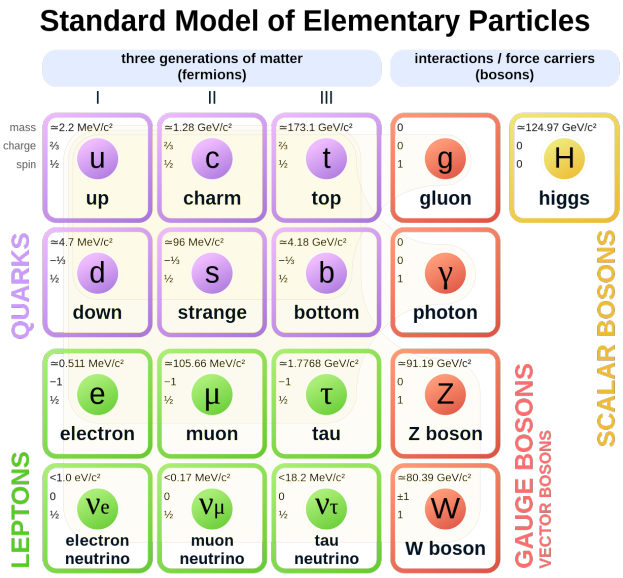

Figure 1.1: The Standard Model categorizes the 17 fundamental particles into 12 fermions and five bosons. For each shown fermion, there is a corresponding anti-fermion that is not represented in this figure. The fermions can be sub-categorized into three lepton generations and three quark generations. Figure taken from [12].

The fermions can be divided into two groups: the quarks and the leptons. There are six quarks and six leptons. For each fermion there is a corresponding anti-particle with opposite charge. The crucial difference between leptons and quarks is the concept of confinement. While leptons can exist freely, quarks are confined to bound states. These bound states are called hadrons and they are color neutral. This confinement is a direct consequence of the quantum chromodynamic (QCD) interaction. However, if the temperature and/or energy density are large enough, quarks can exist freely in the quark-gluon plasma. Despite the experimental efforts which are needed to produce sufficiently large energies, it is of great interest to probe the properties of the QGP, since it allows further insights into the strong interaction. The hadrons can be further separated into mesons, which consist of a quark and an anti-quark, and baryons, which consist of three quarks or three anti-quarks. Quarks and leptons can be split into three generations. Particles in different generations differ from each other only in their mass.

Although a detailed description of the interaction between particles requires a higher understanding of quantum field theory, the basic interactions of the SM can be introduced. There are three types of basic interactions between fermions described by the SM: strong, electromagnetic and weak interaction. These interactions are mediated by bosons. The strong interaction, which is described by QCD, is mediated by the gluon. The electromagnetic interaction is mediated by the photon and the weak interaction is mediated by the neutral Z-boson and the charged $W^{\pm}$-boson.

1.3 Particle detection

The principle of a detector is measuring the interaction of particles with the detector material. Given a relativistic charged particle that passes through the detector material, it will interact electromagnetically with the atomic electrons of the detector material. If the energy is sufficient, the particle

loses energy by ionizing the atoms. The ionisation energy loss per unit length of a particle which traverses a medium with atomic number Z and number density n with velocity $v = \beta c$ is given by the Bethe-Bloch equation [7]:

$$\frac{dE}{dx} \approx -4\pi\hbar^2 c^2 \alpha^2 \frac{nZ}{m_e v^2} \left\{ \ln\left[\frac{2\beta^2\gamma^2 c^2 m_e}{I_e} \right] - \beta^2 \right\}. \tag{1.1}$$

One can express $\beta\gamma$ in terms of mass m and momentum p:

$$\beta\gamma = \frac{v}{c} \cdot \frac{1}{\sqrt{1 - \left(\frac{v}{c}\right)^2}} = \frac{p}{mc}. \tag{1.2}$$

Thus, particles with equal $\beta\gamma$ values but different masses will differ in their momentum and can thus be separated from each other due to their different energy loss. This feature of the Bethe-Bloch equation allows one to identify electrons and separate them from hadrons. In Figure 1.2, one can clearly see the differences in ionisation energy loss per unit length for different particles as a function of the momentum. There are three characteristic regions of the Bethe-Bloch curve. Slower particles with low $\beta\gamma$ have a longer interaction time with the material of the detector and will deposit more energy. For increasing $\beta\gamma$ and decreasing interaction time, the energy deposit will decrease proportional to $1/\beta^2$. The distribution shows a minimum at $\beta\gamma \approx 3 - 4$. Particles in this region are called "minimum ionising particles". For large $\beta\gamma$, one can neglect the β^2 term in equation (1.1) and the energy deposit per unit length increases proportional to $\ln(\beta^2\gamma^2)$. This part of the distribution is called the "relativistic rise" and is due to an increase of the transverse electric field due to Lorentz transformation which leads to an increased contribution from charges at larger distances. The seemingly different behaviour of electrons in Figure 1.2 is due to the fact, that electrons have a low mass and are already in the relativistic rise. In addition to ionisation, for electrons with $\beta\gamma \geq 800$ there are other energy-loss mechanisms present. For this thesis in particular, the mechanism of transition radiation emission is crucial and will be discussed in Chapter 2.2.

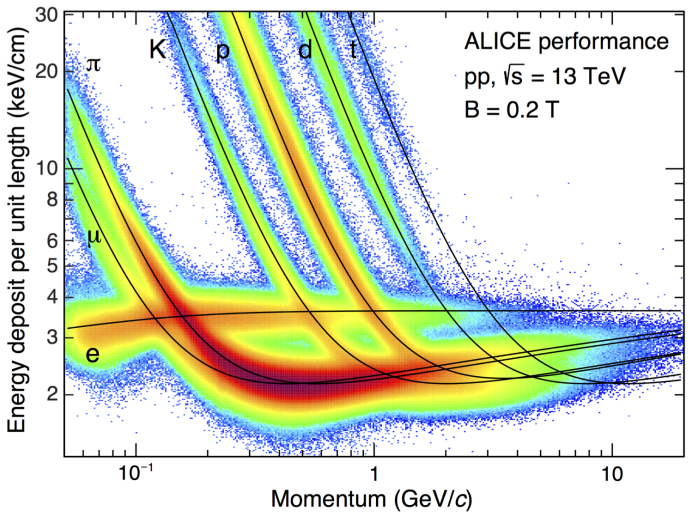

Figure 1.2: Specific ionisation energy loss as a function of the particle momentum in the TPC in pp collisions at $\sqrt{s}$ = 13 TeV. The lines show the expected energy loss given by the Bethe-Bloch equation. Figure taken from [8].

1.4 Outline of thesis

The following Chapter 2 explains the experimental setup of the ALICE Transition Radiation Detector (TRD) and the ALICE Time Projection Chamber (TPC). In Chapter 3, the data samples and the electron trigger conditions of the ALICE TRD will be introduced. The explicit analysis strategy and the trigger efficiency estimation method will be discussed in Chapter 4 and will be compared with previous results of trigger studies in Chapter 5. Lastly, Chapter 6 will give a brief conclusion and outlook.

2 | Detectors

This chapter gives a short overview of the ALICE detector [3]. Since this thesis derives the ALICE TRD electron trigger efficiency, a special focus will be placed on the set up and functionality of the ALICE TRD [11] and the ALICE TPC [5]. The latter will be mainly used for the particle identification.

2.1 The ALICE experiment

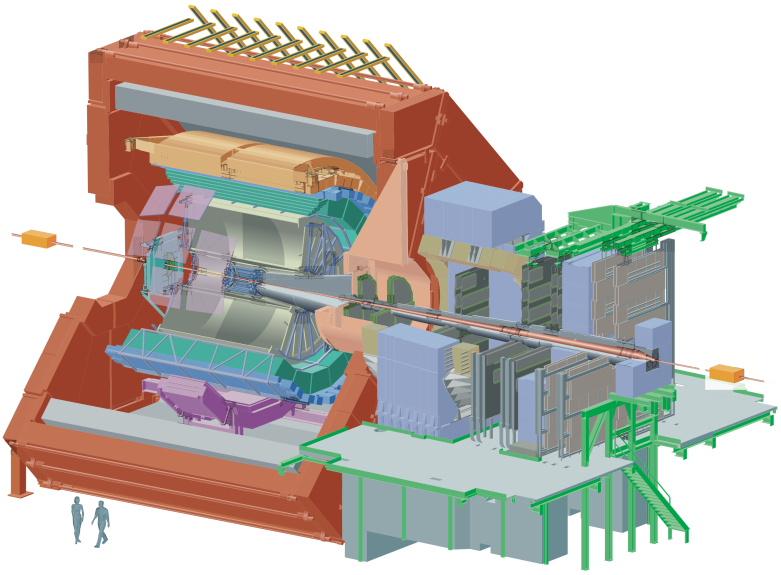

Figure 2.1: Schematic layout of ALICE. Figure taken from [3].

ALICE is one of the four large experiments at the LHC at CERN. It is placed at one of the several collision points of the LHC and is designed to study the physics of strongly interacting matter at extreme energy densities and temperatures created in ultra-relativistic nucleus-nucleus collisions. For this thesis, proton-proton collisions were studied at $\sqrt{s} = 13$ TeV to provide reference data for the heavy-ion program. The dimensions of ALICE are 16m x 16m x 26m with a weight of approximately 10.000t.

ALICE consist of several sub-detectors which are placed around the interaction point. Figure 2.2 shows a cross-section of ALICE and its different sub-detectors.

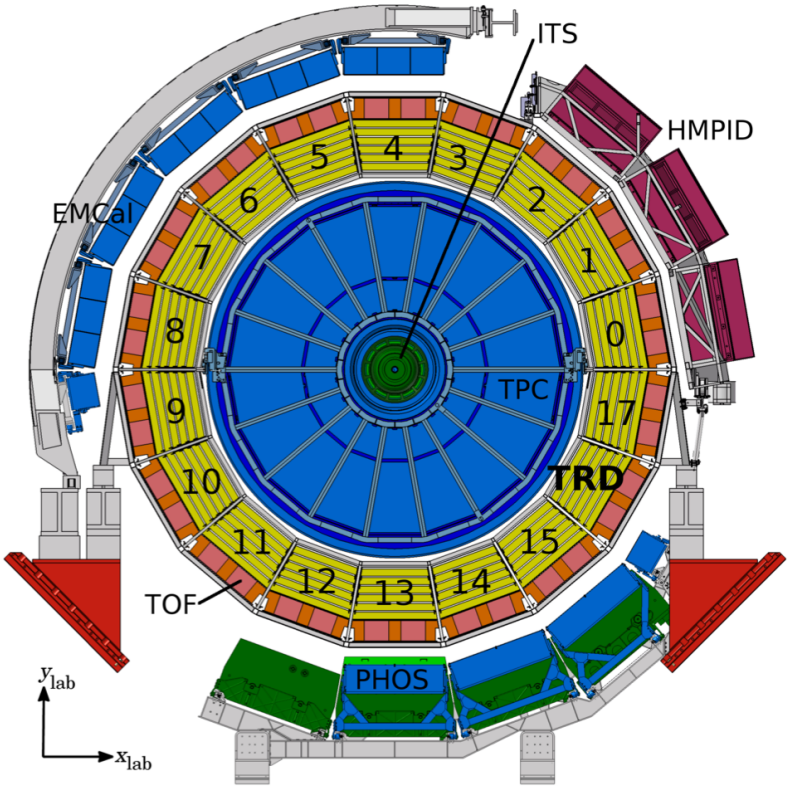

Figure 2.2: Cross section of ALICE. Indicated are the several sub-detectors: ITS, TPC, TRD, TOF, PHOS, EMCal and HMPID. Figure taken from [11].

The individual detectors provide different information needed to reconstruct tracks and energies of the particles that have been produced during the collision and subsequent decays or interactions. The detector closest to the beam is the Inner Tracking System (ITS), made out of planes of high-resolution silicon pixel (SPD), drift (SDD) and strip (SSD) detectors. Then, the Time-Projection Chamber (TPC) follows, which is responsible for particle identification and track reconstruction (see Section 2.3). The Transition Radiation Detector (TRD) and the Time-of-flight detector (TOF) are positioned behind the TPC. All the previously mentioned detectors provide a full azimuth coverage. The electromagnetic caloriemeter (EMCal), the photon spectrometer (PHOS) and the high-momentum particle identification detector (HMPID) are located on the outside of the ALICE detector and do not cover the full azimuth. The central barrel of ALICE is surrounded by a large solenoid magnet with $B = 0.5T$ along the beam direction. The muon arm at forward rapidity used for muon identification and several small detectors used for triggering and event characterisation are not shown in Figure 2.2. As mentioned, the two detectors of relevance for this thesis are the TRD and the TPC. They will be further discussed in the following subsections.

2.2 Transition Radiation Detector

The concept of Transition Radiation (TR) has been predicted in 1945 by Ginzburg and Frank [1]. TR occurs when a particle crosses the boundary between two materials with different dielectric constants. One may think of TR in the following way: a charged particle generates a mirror charge in the medium of the other dielectric constant. Together with the approaching particle charge, this forms a variable dipole that emits photons. For highly relativistic particles ($\beta\gamma \geq 800$ [11]), the emitted photons are in the X-ray domain. Many boundaries are needed to increase the TR yield, since the yield per boundary crossing is of the order of the fine structure constant $\alpha \approx 1/137$. Due to their low mass, electrons can produce TR at momenta around 0.5 $\frac{\text{GeV}}{c}$, while pions start to produce TR at momenta of about 140 $\frac{\text{GeV}}{c}$. This can be used to differentiate between electrons and pions.

As shown in Figure 2.2, the ALICE TRD [11] covers the full azimuth and a pseudorapidity range of $-0.84 < \eta < 0.84$. The pseudorapidity describes the angle relative to the beam axis. The TRD consists of 18 supermodules. Each supermodule is made out of 30 chambers, which are arranged in six layers at a radial distance from 2.90m to 3.68m from the beam axis. Each supermodule is split into five stacks along the beam direction. Figure 2.3 shows the structure of a supermodule.

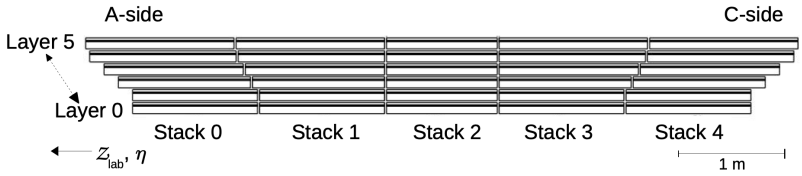

Figure 2.3: Cross section of a supermodule. Each supermodule is split into five stacks, numbered from 0 to 4, and six layers, numbered from 0 to 6. Stack 0 is at the A-side (closer to the magnet door) and stack 4 is at the C-side (closer to the muon arm). Figure taken from [11].

It has to be noted, that there are only 522 chambers installed, because the chambers in stack 2 in the supermodules 13, 14 and 15 were removed in order to minimise the material in front of the photon detector PHOS. Furthermore, over the course of time, some of the chambers broke because of faulty capacitors in the on-detector high-voltage (HV) distribution circuit. This will be further investigated in Chapter 4.

Each chamber of the TRD has the same structure, which is shown in Figure 2.4. First, a radiator is mounted in front of a multi-wire proportional chamber (MWPC) preceded by a drift region. The ALICE TRD uses polypropylene fibre mats as radiator material which are placed between two Rohacell foam sheets. The drift chamber is filled with a Xe-CO_2 (85/15) gas mixture. CO_2 is used as quencher and provides stability against discharges to the detector.

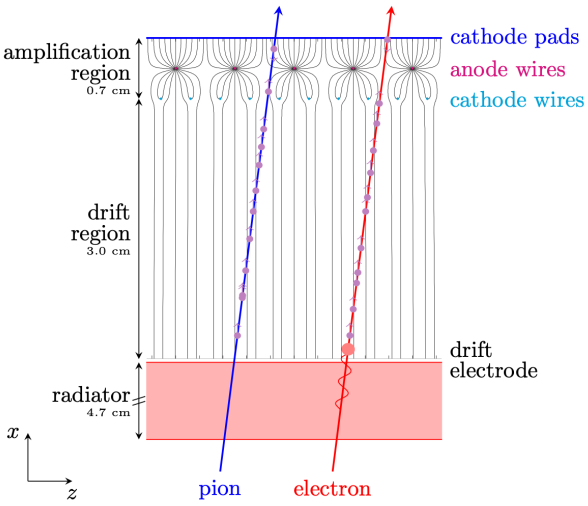

Figure 2.4: Schematic cross section of a TRD chamber perpendicular to the wires. The red dot indicates the large energy deposition due to the TR photon absorption. Figure taken from [11].

Figure 2.5 shows the average pulse height as a function of drift time for pions and electrons (with and without radiator).

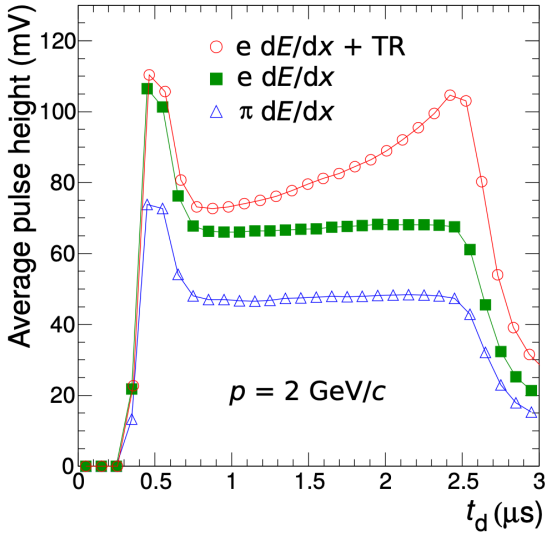

Figure 2.5: Average pulse height as function of drift time for electrons and pions. In case of the electrons, two curves are shown which indicate the case in which the electron traverses radiator material and produces TR (red data points) and the case in which no radiator material is used and thus no TR is produced (green data points). Figure taken from [11].

The first part of the spectrum, arising from the primary charged particle, is identical for the electron and the pion. Then, a constant pulse height can be seen for both particles due to the ionisation trail produced in the drift chamber. However, for the electron with radiator material (red data points), one can see an additional peak due to the TR photon. In order to properly differentiate the individual

peaks, it is important that the TR photon deposits its energy closely after the radiator, which can be ensured by using a high Z gas like xenon.

The produced electrons are then accelerated along the electromagnetic field close to the anode wire. This causes an ionization avalanche which amplifies the signal that is induced on the cathode pads. This region is also called amplification region. The measured TRD signal is readout as a function of time. The individual track segments are calculated online in the on-detector front-end electronics (FEE). From the measured deposited energy loss and a look-up table stored in the FEE, an electron likelihood is obtained. For each stack, a track can be reconstructed based on matched track segments. For each track, a p_{T} and an electron likelihood is calculated. By applying thresholds on p_{T} and the electron likelihood, a single-electron trigger can be derived.

2.3 Time Projection Chamber

The ALICE TPC [5] is the main device for tracking and identifying charged particles. The TPC consists of a hollow cylinder which is parallel to the magnetic field of ALICE. Like the TRD, it is a gas detector. It uses a Ne-CO_2-N_2 gas mixture at atmospheric pressure. If a charged particle traverses the TPC, it will ionize the gas, which causes the ionization electrons to drift to the Multi-Wire Proportional Chambers (MWPC), which are arranged in 18 sectors around each end plate. At the end plates, the special position of the signal deposition in the cylinder plane can be measured which gives a complete trajectory in space, given a measurement of the arrival time.

In this thesis, the TPC is used for particle identification (PID) by measuring the deposited energy loss of the particle and comparing it with the expected energy loss for a particle hypothesis derived from the Bethe-Bloch equation in units of the detector resolution σ:

$$n_\sigma = \frac{\langle \frac{dE}{dx} \rangle_{\text{measured}} - \langle \frac{dE}{dx} \rangle_{\text{theory}}}{\sigma} \tag{2.1}$$

Thus, a smaller n_σ value corresponds to a better agreement of measurement and theoretical prediction of the energy loss of a particle species, e.g. electron. This method will be used in Chapter 4 to identify electrons and differentiate them from hadrons.

3 | Data Sample

The data used for this thesis was collected in 2017 and 2018 in proton-proton collisions at $\sqrt{s} = 13$ TeV. The data can be divided into several data taking periods, which are periods in which the conditions of the beam and the experiment do not change. Each data taking period consists of several runs. Each run contains data that is taken until there is no more beam in the pipe or one of the detectors crashed. In order to be counted as a run, each run has to last at least ten minutes and has to contain information of the SPD, TPC and TRD as readout detectors and of the TRD as a trigger detector. A list of the used data taking periods and the respective runs is given in Appendix B. It should be noted, that the data taking periods LHC18b, LHC18c and LHC17g were excluded from our analysis. For LHC17g and LHC18b, a test trigger has been used, while there is no TRD triggered data available for LHC18c.

3.1 Event selection

Only events that survive the physics selection, an algorithm to reject pile-up, are considered. To ensure that the event is within the geometrical acceptance of the central barrel, the primary vertex position has to be within 10 cm from the nominal center of ALICE. Events with a SPD vertex and a primary vertex reconstructed from global tracks, each with at least one contributor, are selected. In order to be selected, their difference in beam direction has to be smaller than 0.5 cm and the resolution of the z-position of the SPD vertex has to be smaller than 0.25 cm.

3.2 Track selection

For the analysis, tracks with good quality are selected. The applied selection criteria are listed in Table 3.1. The restriction of the pseudorapidity $|\eta|$ was done to match the geometrical acceptance of the TRD. The SPD criterion is set to SPDany to increase the number of electron candidates. In order to remove tracks arising due to material interactions which happen at a larger displacements, cuts on the **D**istance of **C**losest **A**pproach (DCA) are applied. In order to guarantee a high quality of the reconstruction, one requires that a minimum of 70 TPC clusters. The maximum number of TPC clusters is 159. Furthermore, a rejection of kinked tracks, which come from charged mother particles which decay into charged decay products, is applied. As described in [9], the tracks of such particles will suddenly be deflected at the decay point due to different momentum directions of the decay products. The quality of the track reconstruction inside the ITS is quantified by its respective χ^2_{ITS}. To improve the quality of the selected tracks, one requires that χ^2_{ITS} is no larger than 10.

Variable	Criterion
$\|\eta\|$	< 0.84
Require ITS + TPC refit	yes
$N^{\text{TPC}}_{\text{clusters}}$	$\in [70, 160]$
χ^2_{TPC} per cluster	< 4
Reject kink daughters	yes
Require SPDany	yes
χ^2_{ITS} per cluster	< 10
$\|\text{DCA}_{xy}\|$	< 1 cm
$\|\text{DCA}_{z}\|$	< 3 cm

Table 3.1: Track selection criteria

3.3 Monte Carlo sample

Our results will be compared with Monte Carlo (MC) simulations corresponding to about $1.16 \cdot 10^7$ proton-proton collisions. As mentioned before, these data sets are pass2 reconstructions. In order to generate the samples and reflect a realistic particle transport and detector performance, the simulation program PYTHIA [13] was used to simulate the proton-proton collisions and GEANT3 for the particle transport. PYTHIA generates minimum bias events on top of which one J/ψ with a flat rapidity distribution and a natural p_{T} shape was injected. Furthermore, the injected J/ψ has a prompt and non-prompt component. The non-prompt component contains J/ψ as forced decay products of $b\bar{b}$ pairs. The ratio of non-prompt component to prompt component is 3:7. The radiative decay channel of the J/ψ into the dielectron channel is handled via PHOTOS. The TRD trigger is emulated in the simulation applying the same criteria as in data, see Table 3.2.

3.4 TRD trigger conditions

The single-electron trigger applies cuts online on the transverse momentum p_{T}, the PID value, the number of TRD tracklets per track and the sagitta, which is further described in [10]. Also, it requires a hit in the first layer. The values for p_{T} and the PID are calculated online in the **G**lobal **T**racking **U**nit (GTU). More information about the GTU can be found in [2]. The trigger settings are summarised in Table 3.2.

Criterion	Threshold
p_{T} threshold	2 $\frac{\text{GeV}}{c}$ (2 $\frac{\text{GeV}}{c}$)
PID value	130 (165)
Minimum number of TRD tracklets per track	5 (5)
Sagitta cut	0.2 $\frac{\text{GeV}}{c}$ (not applied)
Hit in first layer	required (applied)

Table 3.2: TRD single-electron trigger conditions. The conditions applied in the MC simulations are shown in parentheses.

The distributions of the selection criteria are compared for minimum bias and TRD triggered data as well as MC simulations in Appendix A.1. It is important to mention that in the distributions for the TRD-triggered events, there are tracks which do not fulfill certain trigger conditions, e.g. tracks

with lower PID or p_{T} values. These underlying contributions are produced, if a particle satisfies the trigger conditions while simultaneously another particle with a low momentum or low PID value passes the detector in the same event. Thus, there are entries, e.g. for momenta smaller than 2 $\frac{\mathrm{GeV}}{c}$. These tracks are responsible for a non-vanishing efficiency for momenta smaller than 2 $\frac{\mathrm{GeV}}{c}$ as shown, e.g. in Figure 5.1.

3.5 V0 data sample

The V0 data sample contains electrons from photon conversions in the detector material, pions from K_S^0 decays and protons from Ω decays. The process of photon conversion resembles the characteristics of "V0 particle decays" [6]. As heavy, unstable subatomic particles with neutral charge, the V0 particles are a useful tool for the calibration of the particle identification of the TPC. The decay products of V0 particles lead to purer samples, compared to the physics data sample that has a large background contribution due to hadrons. Furthermore, the particle identification can be done entirely by analysing the decay topology and the invariant mass of the V0 particle. Typical V0 particles are Λ^0 baryons and K_S^0 mesons. Since the K_S^0 mesons decay into two pions, one can use this for a pion-calibration. The Λ^0 baryon decays into a pion and a proton, which makes the Λ^0 suitable for the proton-calibration. Since V0 particles decay via the weak force into two daughter particles with opposite charge, one can identify a decayed V0 particle in, e.g. a bubble chamber, by a V-shaped structure. Figure 3.1 depicts the decay of the Λ^0 baryon, originating from an Ω^-. One can clearly see the V-shaped structure formed by the pion and the proton.

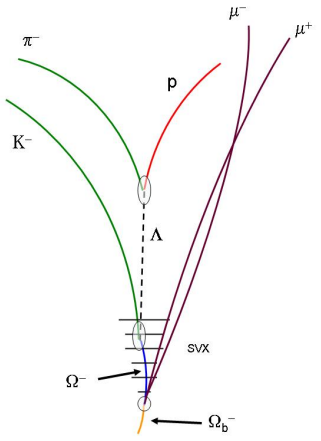

Figure 3.1: Decay of an Ω^- into a Λ^0 and a K^-. The resulting decay products of the Λ^0, the proton and the pion, have opposite charge and form a V-shaped structure. Figure taken from [4].

The identification of the V0 particles is implemented in the ALICE software framework . Although the photon is not in the literal sense a V0 particle, one can use identical methods for the identification of the decay products (electron and positron). The V0 data sample can thus be used for electron calibration, which will be used in Chapter 4.

4 | Trigger efficiency analysis

In this chapter, the method for estimating the TRD electron trigger efficiency is presented. The presented method is then compared with data that has previously been subjected to electron selection and hadron rejection criteria. The final efficiency is then calculated using a runwise analysis, which allows to study the dependence of the efficiency on various external variables.

The electron trigger efficiency is given as the ratio of the number of electron candidates in minimum bias events which also satisfy the trigger condition of the TRD to the number of electron candidates in minimum bias events [14]:

$$\epsilon_{\mathrm{TRD}} = \frac{N_e^{\text{minimum bias events which satisfy trigger conditions}}}{N_e^{\text{minimum bias events}}} \tag{4.1}$$

It should be noted that in the course of this thesis, the terms "TRD triggered" and "satisfying the trigger conditions of the TRD" are used synonymously. The single-electron trigger efficiency is studied differentially as a function of the transverse momentum, the azimuth angle ϕ, the pseudorapidity η, the gain and the data taking period. One needs to take into account that our data samples include contributions from hadrons, such as pions and protons. In Figure 4.1, the TPC n_σ, defined in equation (2.1), for the electron hypothesis is plotted against the transverse momentum p_{T}.

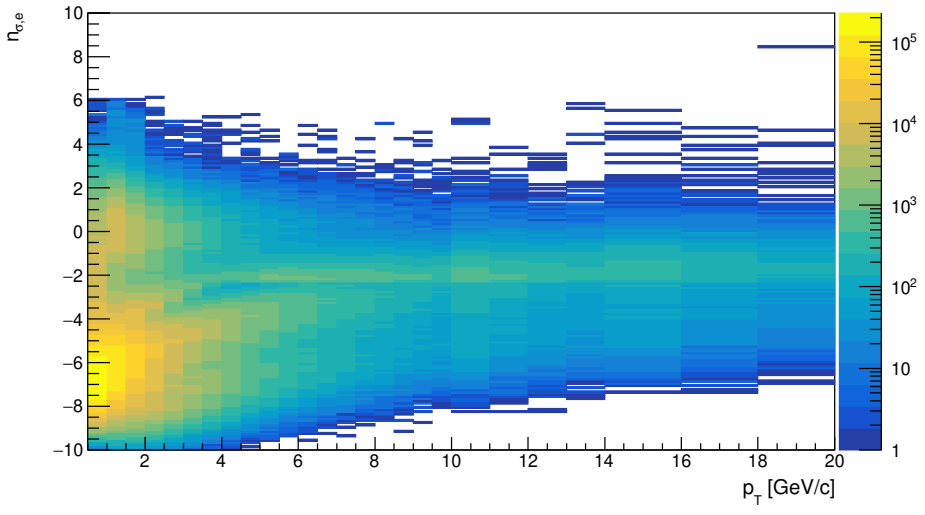

Figure 4.1: TPC $n_{\sigma,e}$ for the electron hypothesis as a function of the transverse momentum for the minimum bias data sample.

There is a significant amount of entries located around $-8 < n_{\sigma,e} < -4$ at momenta up to $p_{\mathrm{T}} = 6\ \frac{\mathrm{GeV}}{c}$ that arise due to the contributions of pions and protons. A hadron rejection has already been applied while filling the trees in order to downscale the hadron contributions for $n_{\sigma,e} < -2$ [15]. The electron contribution is centered around $n_{\sigma,e} = 0$. Since only the electron signal is of interest, one restricts the further analysis to $-3 < n_{\sigma,e} < 3$. However, the hadron contamination in this interval increases with transverse momentum, because the energy loss of the hadrons "enters" the regime of the relativistic rise and approaches a similar energy loss as the one of electrons (see Figure 1.1). Thus, the residual hadron contamination has to be subtracted using the approach described below. In order to counteract statistical fluctuations, the momentum bin size increases for higher momenta.

4.1 Estimation of the hadron contamination

As mentioned, it is important to correct our data for hadron contamination. In this sub-chapter, the method used for determining the hadron contamination is presented. Furthermore, it is tested if simple electron selection and hadron rejection criteria can be introduced to deliver similar results as our method and thus used for further investigations.

One-dimensional projections of each p_{T} bin on $n_{\sigma,e}$ allow to quantify the hadron contribution to the electron signal for each p_{T} bin. Figure 4.2 shows two exemplary projections for $p_{\mathrm{T}} = 3.5 - 4\ \frac{\mathrm{GeV}}{c}$ and $p_{\mathrm{T}} = 5.5 - 6\ \frac{\mathrm{GeV}}{c}$.

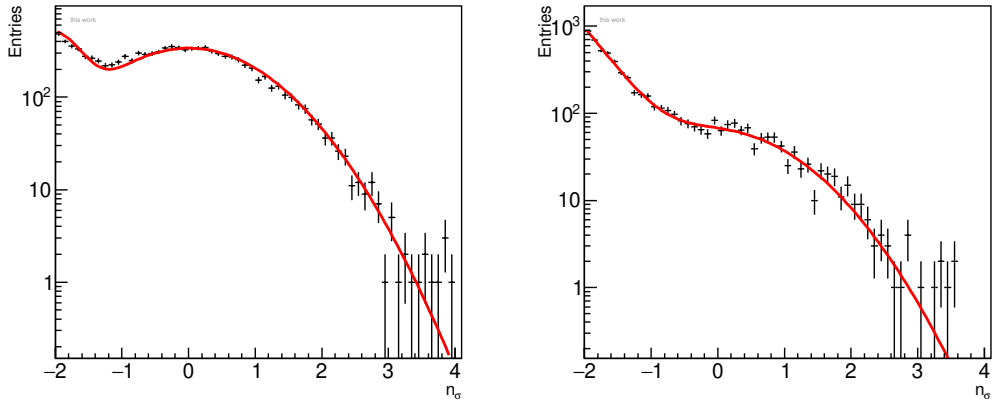

Figure 4.2: Distributions of $n_{\sigma,e}$ for $3.5 < p_{\mathrm{T}} < 4\ \frac{\mathrm{GeV}}{c}$ (left) and $5.5 < p_{\mathrm{T}} < 6\ \frac{\mathrm{GeV}}{c}$ (right). The red curve indicates the fit function given by two gaussian distributions

There are distinct regions which can be identified either as originating from hadrons or electrons. The expected electron signal in centered at $n_\sigma \approx 0$. The applied hadron rejection while filling the trees leads to the rather unexpectedly narrow gaussian structure located at $n_\sigma \approx -2$, which resembles the contributions of the pions.

In order to correctly determine the hadron contamination, one has to determine the number of entries that the hadrons contribute to the electron signal. First, a gaussian distribution is fitted to the electron signal. The hadron signal can be fitted with a single gaussian distribution as well, since for low momenta only pions are contributing to the hadron signal, while for high momenta the proton contribution overlaps with the pion contribution. In order to constrain the parameters of the fit functions,

the n_σ-distributions for electrons from photon conversion and pions from K^0_S decays (V0 data sample) were fitted using gaussian distributions. As an example, Figure 4.3 shows the fit results for the mean and width (sigma) of the gaussian fit for electrons as a function of the transverse momentum.

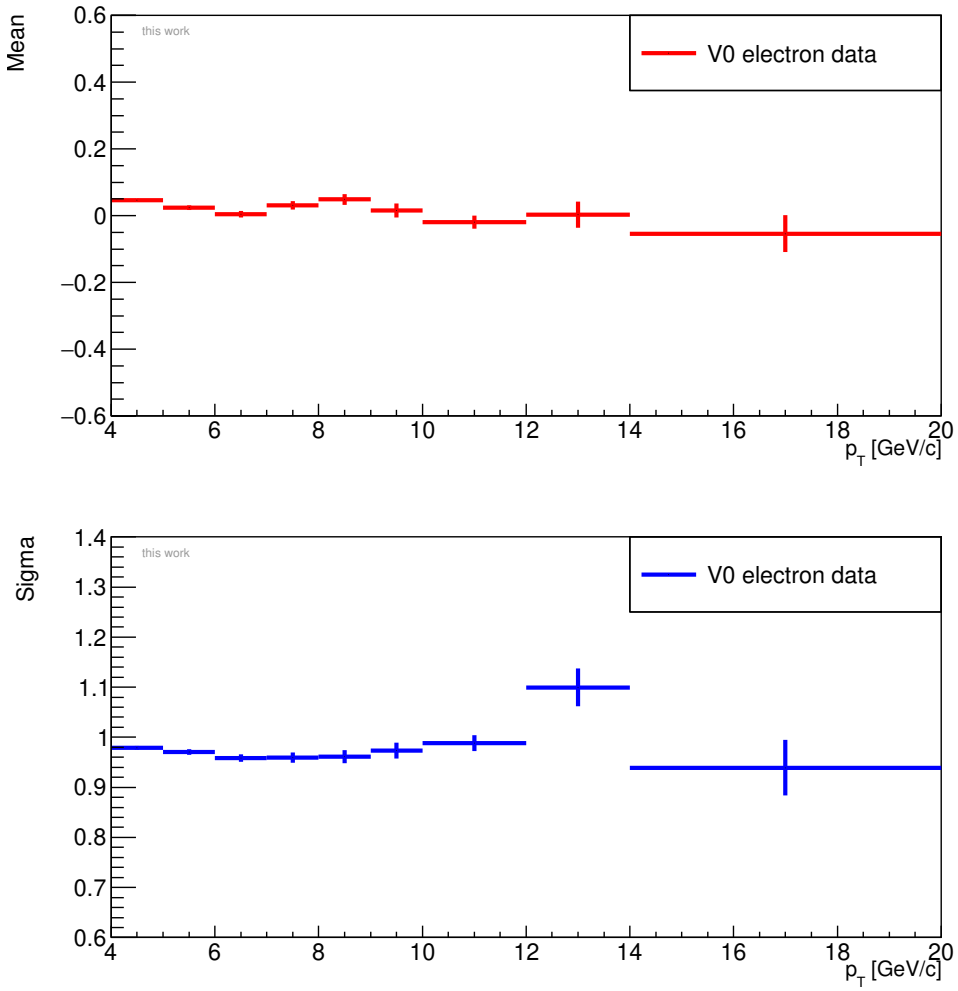

Figure 4.3: Mean and width (sigma) of the gaussian fit to the $n_{\sigma,e}$ distribution in momentum bins for electrons from photon conversions (V0 data sample). The errors shown result from the calculated errors of the gaussian fit.

The mean and the width of the gaussian are centered around zero and one, respectively. Thus, these parameters may be fixed for the electron gaussian fit.

Given the two fit functions for the electron and the pion, the hadron contamination can be determined by calculating the shared area of the two fit functions. The shared area is a measure of how many hadrons have a $n_{\sigma,e}$ value similar to the electron in a given $n_{\sigma,e}$ range. Three different electron identification selection criteria (cuts) will be introduced. By applying the cuts, one is not looking at the total area shared by the two fit functions, but only a certain area which is defined by the cut. For example, if one uses the cut $0 < n_\sigma < 3$, one is only interested in the area shared between the fit

functions from $0 < n_\sigma < 3$. Logically, if one uses a larger cut range, e.g. $-1 < n_\sigma < 3$, the shared area and therefore the hadron contamination will be larger. The hadron contamination C can then be calculated as the following ratio:

$$C_{x<n_\sigma<3} = \frac{\text{Shared area of electron and pion distribution in the range of } x < n_\sigma < 3}{\text{Area of the total distribution in the range of } x < n_\sigma < 3}. \tag{4.2}$$

In this thesis, cuts with $x = -1$, $x = -0.5$ and $x = 0$ are used. The determined hadron contamination for each cut is presented in Figure 4.4.

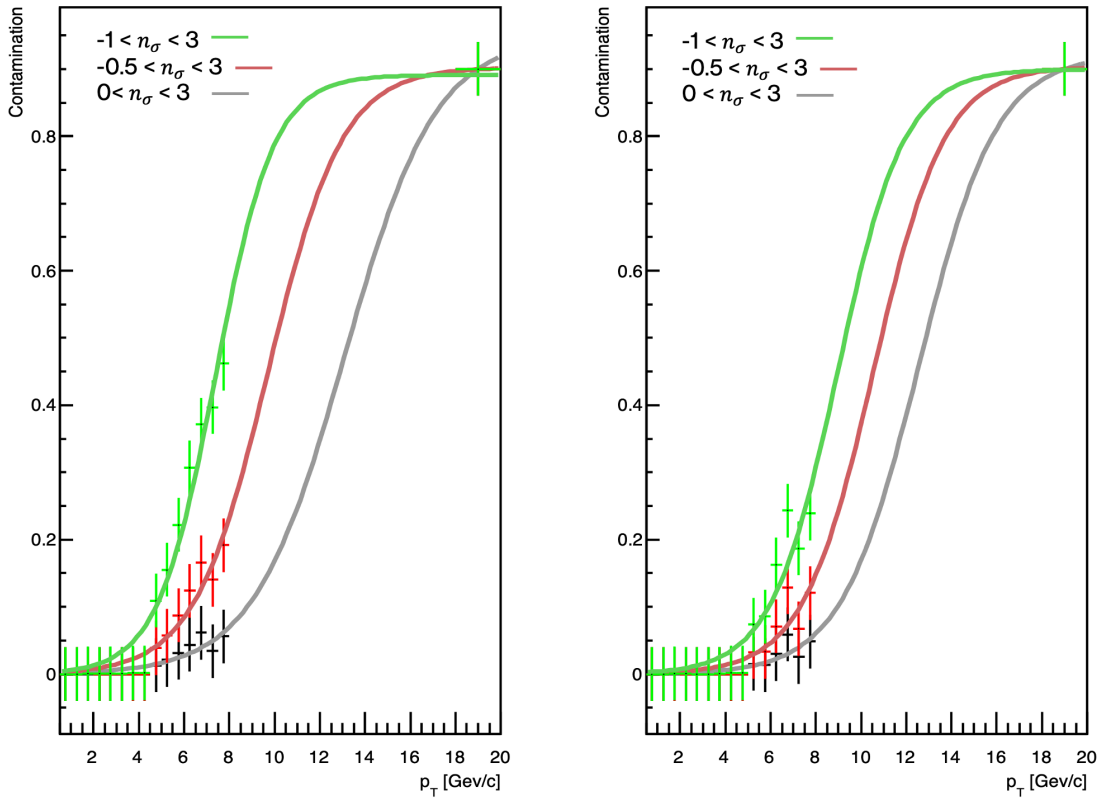

Figure 4.4: Left: Hadron contamination for three different electron identification selection criteria (cuts) for electrons in the minimum bias data sample as a function of p_T. Right: Hadron contamination for three different electron identification selection criteria (cuts) for electrons in the TRD triggered minimum bias data sample as a function of p_T. This data sample contains events that are readout, because they a minimum bias events, but the events also fulfill the TRD trigger conditions. In both cases, the errors shown are fixed to 0.04.

Only the hadron contamination for electrons is shown, since the hadron contamination for positrons is assumed to be the same. For momenta higher than $p_T = 8 \frac{\text{Gev}}{c}$, the signal can not be adequately described by two gaussians fits. This is because the contributions from protons and pions overlap with a large fraction of the electron signal, which makes the fitting of two gaussian distributions difficult. In order to get satisfactory results, the hadron contamination was determined via the aforementioned method up to $p_T = 8 \frac{\text{Gev}}{c}$ and was fixed to 90% for $p_T = 18 \frac{\text{GeV}}{c}$, i.a. the highest p_T bin. Then, an error function can be used to fit the data points. As seen in Figure 4.1, the hadron contribution increases for $n_{\sigma,e} < 0$. Thus, if one chooses a cut which extends into regions of $n_{\sigma,e} < 0$, the

hadron contamination will increase. This behaviour can be seen in both plots of Figure 4.4, e.g. for the green curve with $-1 < n_{\sigma,e} < 3$ which shows a higher hadron contamination than the grey curve with $0 < n_{\sigma,e} < 3$. Also, the minimum bias data (left plot) show a higher level of hadron contamination than the minimum bias data that also fulfills the TRD trigger conditions (right plot). This is expected, since the TRD trigger is supposed to trigger on electrons and not on hadrons. This improves the signal-to-background ratio for electrons. Additionally, the hadron contamination is small for low p_{T}. This is due to the fact that the method of simply applying a n_{σ}-restriction is sufficient for low p_{T}, since the pions are not yet in the relativistic rise.

It is of interest to study the efficiency as a function of the transverse momentum p_{T}. Therefore, one performs one-dimensional projections for each of the three cuts on p_{T}. This allows to calculate the number of electron candidates as a function of p_{T} for a given electron identification selection criterium. Since the shared area is different for each of these cuts, one has to correct the p_{T} spectra with the "cut efficiency" in order to compare the individual p_{T} spectra for each electron selection criteria with each other. The cut efficiency is given as the integrated gaussian fit function for the electron from the lower boundary of the cut to infinity. For example, since the used gaussian fit function for the electron distribution is centered at zero and has a width of one, the cut efficiency for the cut $0 < n_{\sigma} < 3$ is given as the integral of the gaussian fit from zero to infinity, which yields 0.5. Choosing a cut with a lower boundary value, e.g. $-1 < n_{\sigma} < 3$, increases the cut efficiency. After correcting for the cut efficiency and subtracting the hadron contamination, the p_{T} spectra for each cut should overlap. Thus, the different electron identification selection criteria can be used as tools to check our hadron rejection method. To correct a p_{T} spectrum for hadron contamination, one has to multiply the p_{T} spectrum with the contamination fit function and then subtract this modified spectrum from the raw spectrum. The corrected p_{T} spectra for the three different electron identification selection criteria are shown in Figure 4.5 for the minimum bias data sample (left) and the TRD triggered minimum bias data sample (right):

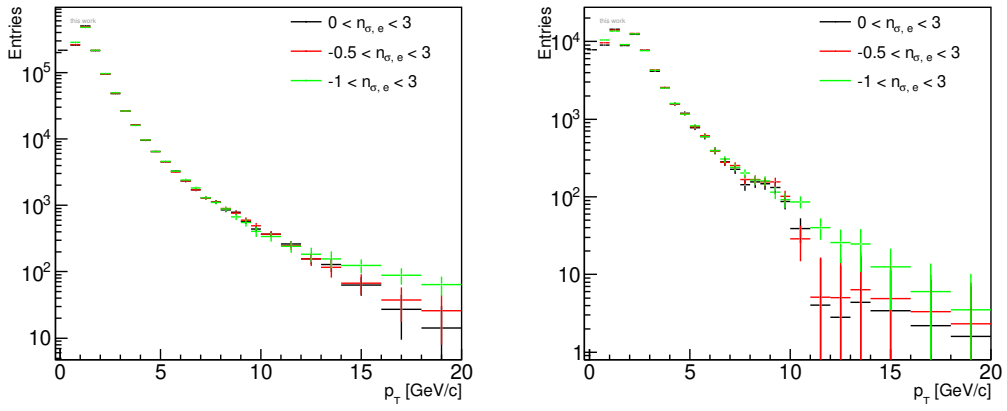

Figure 4.5: Left: Corrected p_{T} spectrum for the minimum bias data sample for each electron identification selection criteria. Right: Corrected p_{T} spectrum for the TRD triggered minimum bias data sample for each electron identification selection criteria.

The momentum threshold at $p_{\mathrm{T}} = 2\ \frac{\mathrm{GeV}}{c}$ is reproduced in the p_{T} spectra. Entries below the threshold arise due to underlying events. For momenta up to $p_{\mathrm{T}} = 8\ \frac{\mathrm{Gev}}{c}$, the p_{T} spectra for each cut overlap perfectly. This verifies, that the above explained hadron rejection method is good. For larger transverse momenta, where the hadron contamination was extrapolated, the spectra for the three cuts

deviate stronger. This indicates that the hadron rejection gets worse for larger transverse momenta, which suggests that the extrapolation at higher momenta fails to describe the hadron contamination adequately. Especially for the TRD triggered minimum bias data sample (right plot of Figure 4.5), the spectra deviate strongly from each other for $p_{\mathrm{T}} > 10\ \frac{\mathrm{GeV}}{c}$. Since the TRD triggered minimum bias data sample is a subset of the minimum bias data sample and thus has less entries, these deviations are also due to insufficient statistics at larger momenta.

The efficiency is then given as the ratio of the corrected p_{T} TRD triggered minimum bias spectrum to the corrected p_{T} minimum bias spectrum, as mentioned in equation (4.1). Figure 4.6 shows the determined efficiency for the cut $0 < n_\sigma < 3$ as a function of the transverse momentum for positrons and electrons. For this thesis, the trigger efficiency is only determined for the cut $0 < n_\sigma < 3$ in order to limit oneself as much as possible to the contribution of electrons. For the electrons, a simple error function can be used to fit the efficiency curve. For the positrons however, two error functions seem to describe the slope behaviour better. The slower rise of the positron efficiency can be led back to the ExB effect.

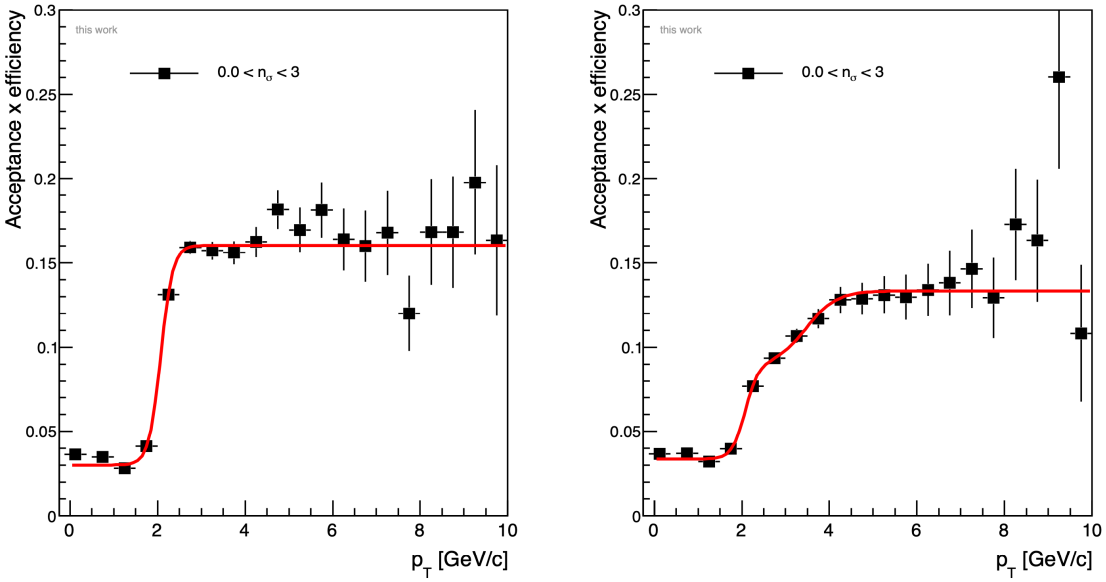

Figure 4.6: Efficiency of the TRD trigger for electrons (left) and positrons (right) as a function of p_{T}. The red curves represent the in the text described fit functions. Since the efficiency is calculated by dividing two correlated histograms, binomial errors have been used.

The determined efficiencies nicely reproduce the expected sharp onset due to the p_{T}-trigger-threshold at $2\ \frac{\mathrm{GeV}}{c}$. For $p_{\mathrm{T}} < 2\frac{\mathrm{GeV}}{c}$, the efficiencies show an offset from zero. This can be explained by the presence of underlying events, e.g. electrons with low momentum that do not fulfill the trigger conditions but are part of an event that was triggered by electrons or positrons that do fulfill the trigger conditions. For both charges, the efficiency of the TRD reaches a plateau. This plateau is around 16% for electrons and around 14% for the positrons. At high momenta, the uncertainties get large due to statistical fluctuations and possibly remaining hadron contributions.

4.1.1 Comparison with modified data sets

In order to reduce the amount of code and simplify the further analysis, one can check if a hard PID hadron rejection cut delivers equivalent results as the method previously described. Therefore, one applies TPC n_σ cuts on the electron ($0 < n_{\sigma,e} < 3$) and tight hadron rejection cuts on the pion ($n_{\sigma,\pi} > 3.5$) and the proton ($n_{\sigma,p} > 3.5$). Figure A.6 shows the resulting TPC n_σ for the electron hypothesis as a function of p_T. The efficiency can be determined analogously to the method described in Sub-Chapter 4.1 by performing one-dimensional projections on p_T and dividing the TRD triggered minimum bias spectra by the minimum bias spectra. The trigger efficiencies for positrons and electrons after applying the electron selection and hadron rejection criteria are presented in Figure 4.7.

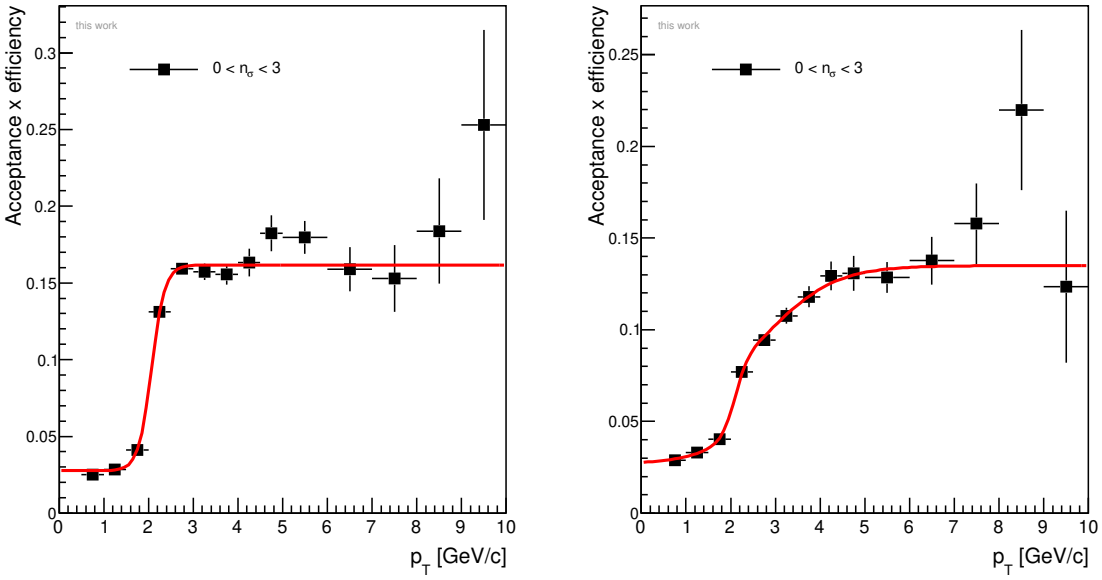

Figure 4.7: Efficiency of the TRD trigger for positrons and electrons as a function of p_T after applying selection criteria for electron identification and hadron rejection. The shown errors are binomial errors.

The trigger efficiencies show the expected onset due to the p_T-trigger-threshold and reproduce the ExB effect well. Furthermore, the efficiency reaches a plateau for both charges. The plateau is around 16% for electrons and around 14% for the positrons, which corresponds perfectly to the plateau value of the efficiencies estimated using the hadron fit method. For increasing momenta, the uncertainties due to statistical fluctuations and remaining hadron contributions increase as well. Since the application of electron selection and hadron rejection criteria produces similar efficiencies as the previously described method, the further analysis is done using these selection and rejection criteria because it simplifies the amount of needed code and reduces possible errors within the code.

4.2 Runwise efficiency

Until now, minimum bias data has been used in order to determine the trigger efficiency of the TRD. However, the physics analyses of interest use TRD-triggered data. Furthermore, the efficiency of the TRD depends on the gain. Since changes in gain result in changes of the measured energy loss, the cut on the PID value has a different effect if one keeps the PID threshold constant. In order to account for both of these things, this thesis follows the same approach that has been used in [14].

One has to perform a runwise analysis. First, for each run the corresponding gain has to be determined. The gain for each TRD chamber is determined on a runwise basis and the average gain value for all chambers is stored in the OCDB database for each run. Runs with the same average gain value are stored in the same "gain category" [14]. The respective runs that fall into each gain category are shown in Figure A.8.

For each run, a p_{T} spectrum can be extracted. Then, one sums up all spectra of the same gain category. This allows to study the efficiency as a function of the gain category by dividing the TRD triggered minimum bias spectra by the minimum bias spectra. For each gain category, the mean efficiency was determined using a polynomial fit of degree zero in the efficiency-plateau region $p_{\mathrm{T}} = 3 - 6\ \frac{\mathrm{GeV}}{c}$. The fit result for each gain category is plotted in Figure 4.8.

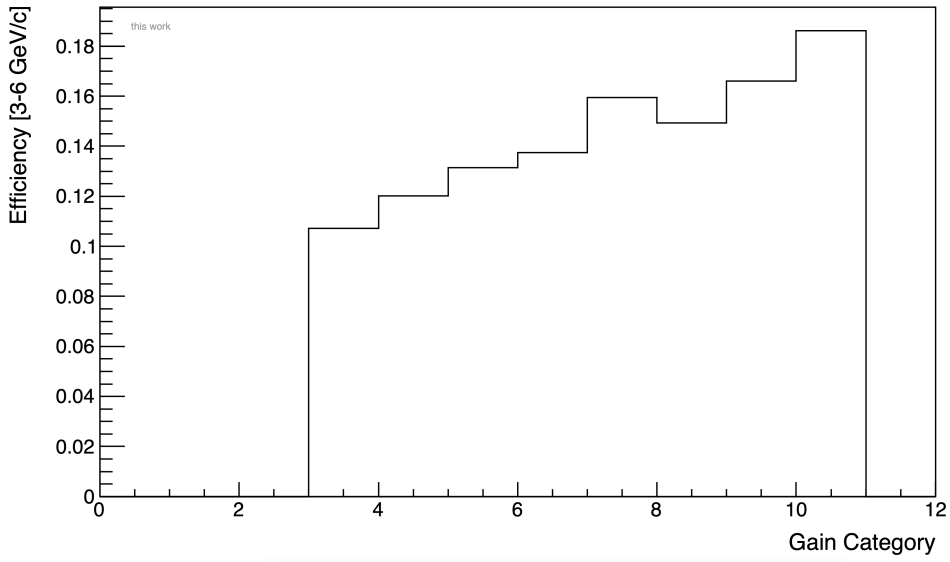

Figure 4.8: Efficiency of the TRD as a function of the gain category. This is for both charges combined.

The efficiency depends as expected linearly on the gain, i.e. the efficiency increases with gain.

To find the final efficiency, one has to be aware that the number of minimum bias events per run is not the same as the number of TRD triggered events. The number of entries per run for the TRD sample can be found in Appendix A.9. The final spectra are obtained by summing up the p_{T} spectra of the individual gain categories, using the number of TRD events for each gain category as a weight. Finally, one divides the weighted and summed TRD triggered minimum bias p_{T} spectrum by the weighted and summed minimum bias spectrum. The final result is shown in Chapter 5.

4.3 Differential analysis of the efficiency

It is important to study the variations of the efficiency. Thus, the dependence of the efficiency on time and location within the TRD detector setup will be investigated. Possible influences on the efficiency are, i.a. changes in the used gas mixture or broken detector parts.

The Xe-CO_2 ratio is not constant. Figure 4.9 shows measurements of the Xe-$C0_2$ ratio from the gas chromatograph.

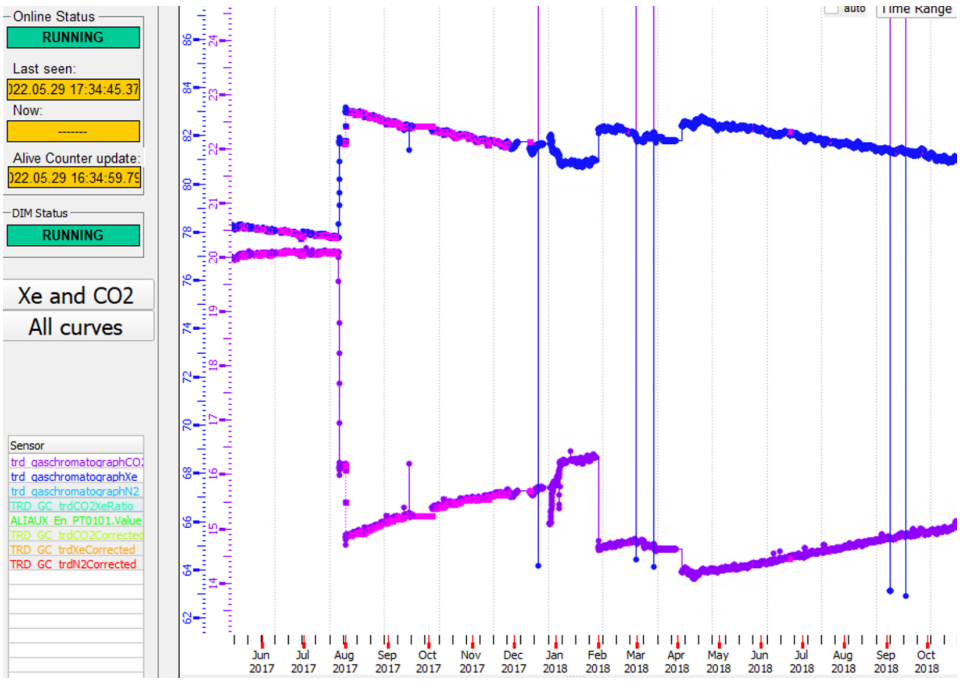

Figure 4.9: Data from the gas chromatograph for Xe and CO_2 as a function of time. The data points in magenta represent the measurements for Xe and the blue data points represent measurements for CO_2. Figure taken from [15].

For the months of June and July in 2017, there was too little xenon which resulted in an approximate Xe-CO_2 ratio of 78/20. Only at the beginning of August, additional xenon was injected and the Xe-CO_2 ratio went back up to approximately 84/15. Then, over the course of seven months up to February of 2018, the Xe-CO_2 ratio declined linearly before the it was readjusted again. In the following months of 2018, the amount of xenon decreased linearly. A decline in xenon results with a constant high voltage in a deterioration in gain and in a worse separation of the signal from the primary charged particle and the TR photon, as described in 2.2. Thus, one expects that during the months of June and July in 2017, the TRD was insufficient in differentiating the electron and pion signals which leads to a worse electron efficiency. To investigate the effect, the efficiency is determined for each data taking period. The mean efficiency for each data taking period is determined by fitting a polynomial of degree zero to the p_T-differential efficiency in the interval of $p_T = 3 - 6 \frac{GeV}{c}$. This p_T range is chosen, since it guarantees that one uses the maximum plateau value of the efficiency curve, as shown in Appendix A.10. The result of this procedure can be seen in Figure 4.10.

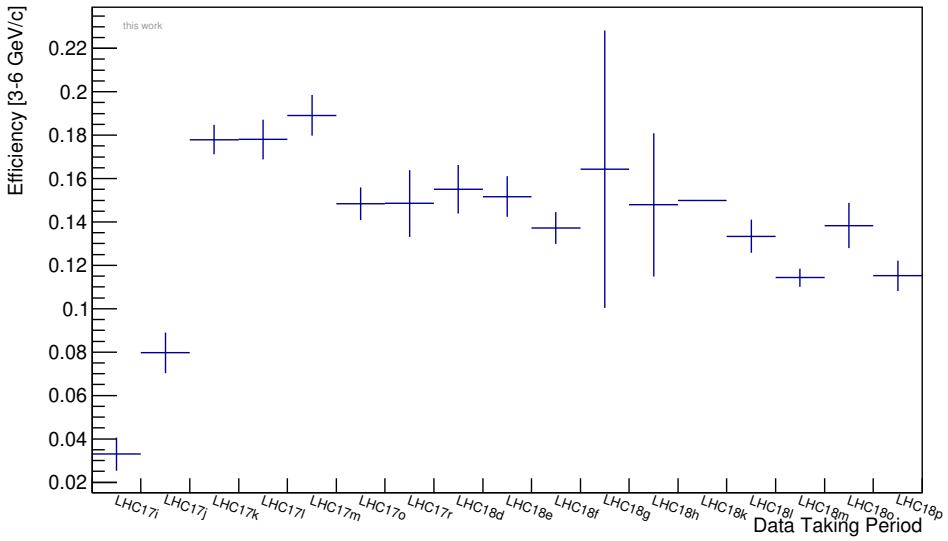

Figure 4.10: Efficiency of the TRD as a function of the data taking period. The mean efficiency of each data taking period was determined in the range of $p_{\mathrm{T}} = 3 - 6\ \frac{\mathrm{GeV}}{c}$. This result is for both charges combined. The errors shown result from the calculated errors of the polynomial fit.

If one compares Figure 4.10 with Figure 4.9, strong similarities can be found. For the data taking periods LHC17h and LHC17i, the efficiency is lower since there is too little xenon in the gas mixture. This leads to a lower gain and thus a lower efficiency. A strong increase in efficiency can be seen during the data taking period LHC17j, which is the result of the xenon injection and thus a higher efficiency. However, there was too much xenon for the periods LHC17k and LHC17m, which resulted in efficiencies larger than expected. Once the nominal Xe-CO_2 ratio is reached, the efficiency is constant until LHC18h, whereafter the effects of the linear decrease of xenon can be seen in the efficiency as well. A strong correlation between the Xe-CO_2 ratio and the efficiency is observed. Therefore it is important to keep the gas mixture as constant as possible in the future.

In order to study the dependence of the TRD electron trigger efficiency on the location within the TRD detector setup, the efficiency as a function of the azimuth ϕ and the pseudorapidity η is investigated. To do so, one applies the outlined electron identification and hadron rejection selection criteria and performs a two-dimensional projection of $p_{\mathrm{T}} = 6 - 10\ \frac{\mathrm{GeV}}{c}$ on η and ϕ. The efficiency is then determined as the ratio of the TRD triggered minimum bias sample to the minimum bias sample. The efficiency as a function of η and ϕ is plotted in Figure 4.11.

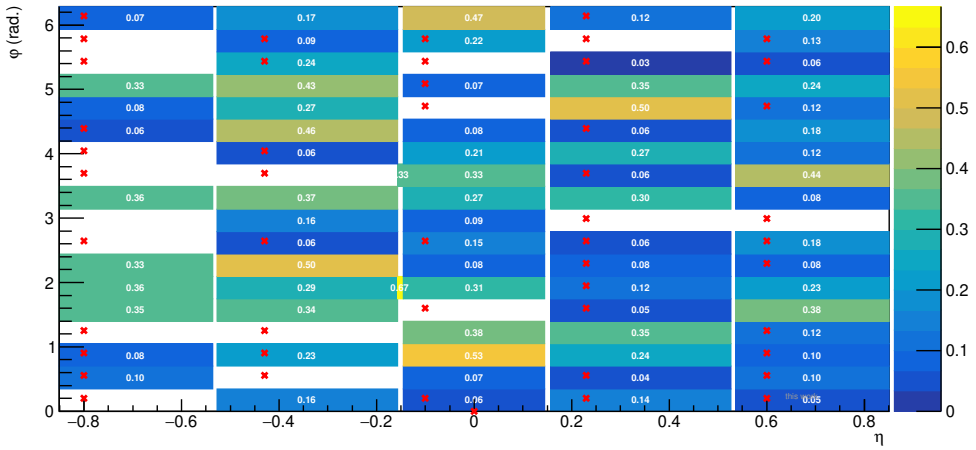

Figure 4.11: Electron efficiency of the TRD as a function of the azimuth ϕ and the pseudorapidity η for the momentum range $p_{\mathrm{T}} = 6-10\ \frac{\mathrm{GeV}}{c}$. The red crosses indicate that the corresponding stack did not fulfill the trigger criteria due to malfunctioning hardware (HV, front-end electronics) at the end of 2018.

The resulting ratio is written inside each stack. The several empty stacks are due to the fact that some of the stacks don't fulfill the trigger conditions due to malfunctioning hardware (HV, front-end electronics). Thus, e.g. the first layer was not hit or the minimum number of functioning chambers per stack was less than five. Some of the chambers broke down over the course of 2017 and 2018 which results in a smaller than average efficiency. The red crosses indicate stacks which did not fulfill the trigger conditions at the end of 2018. These stacks can be identified by analyzing the hardware status of each supermodule at the end of 2018, given by Figure in Appendix A.7. Thus, there are non-negligible deviations between the individual stacks. This is not optimal, since the trigger efficiency should not depend on the location within the TRD detector setup. Possible explanations are either the broken chambers that reduced the efficiency and the fact that the track parameters η and ϕ are determined at the vertex. The latter leads to deviations especially in the low momentum region, since the tracks of the particles curve due to the magnetic field and thus the η and ϕ of the particle arriving at the TRD are different to the values determined directly at the vertex. This effect can be evaded by choosing higher momentum ranges, since the radius of the curvature is proportional to the momentum. Thus, the deviations from the determined values at the vertex and the TRD are smaller.

5 | Results and Comparison

In this chapter, the determined TRD electron trigger performance for proton-proton collisions at $\sqrt{s} = 13$ TeV will be presented and compared with the trigger performance determined by Y. Pachmayer [15] for proton-lead collisions at $\sqrt{s} = 8.16$ TeV, recorded in 2016.

5.1 Final TRD trigger performance

The strategy for the determination of the TRD trigger efficiency is described in Sub-Chapter 4.2. Figures 5.1 and 5.2 show the final electron and positron trigger efficiency of the ALICE TRD as a function of the transverse momentum in proton-proton collisions at $\sqrt{s} = 13$ TeV. As a comparison, the ALICE TRD trigger efficiency in Monte Carlo simulations has also been determined.

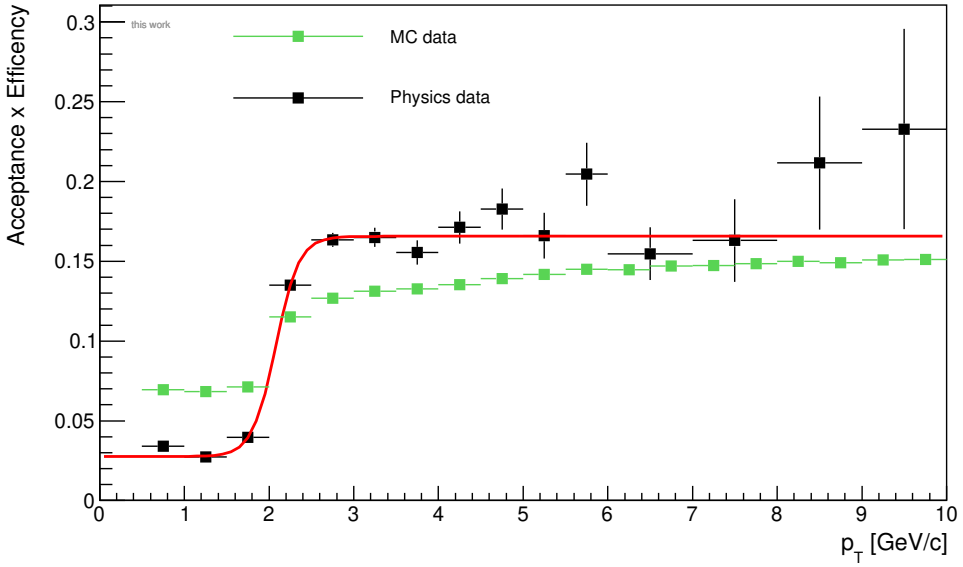

Figure 5.1: Electron trigger efficiency of the ALICE TRD in proton-proton collisions at $\sqrt{s} = 13$ TeV for physics data and Monte Carlo simulations. Also shown is the fitted error function in red for physics data. The shown errors are binomial errors.

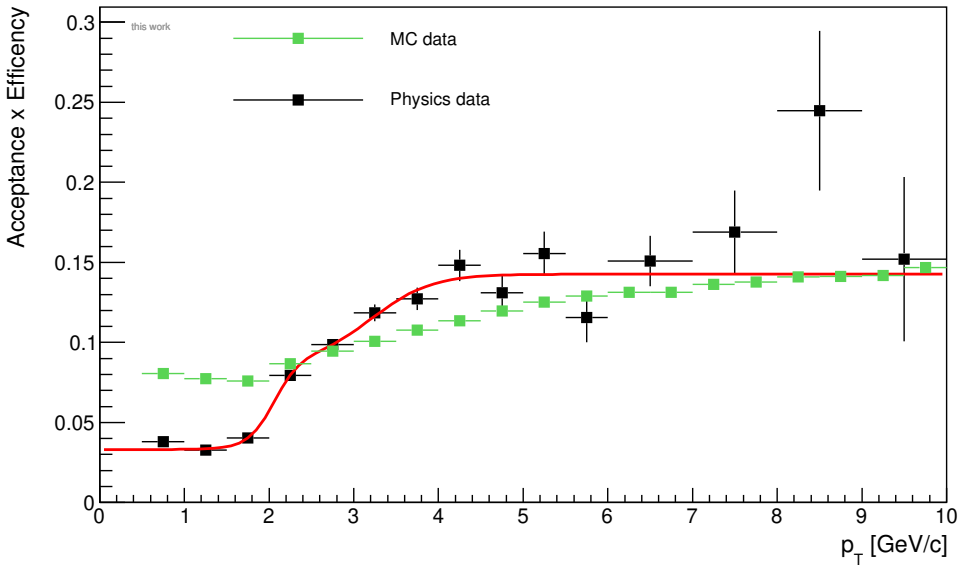

Figure 5.2: Positron trigger efficiency of the ALICE TRD in proton-proton collisions at $\sqrt{s} = 13$ TeV for physics data and Monte Carlo simulations. Also shown is the fitted error function in red for physics data. The shown errors are binomial errors.

The calculated efficiencies for the physics data show the expected sharp on-set for $p_{\mathrm{T}} \approx 2\ \frac{\mathrm{GeV}}{c}$ due to the p_{T}-threshold, as well as the different rise for the both charges due to the ExB effect. The efficiency reaches a plateau of approximately 17% for electrons for $p_{\mathrm{T}} > 2.5\ \frac{\mathrm{GeV}}{c}$ and 15% for positrons for $p_{\mathrm{T}} > 5\ \frac{\mathrm{GeV}}{c}$. Furthermore, the non-zero trigger efficiencies for momenta smaller than the p_{T}-threshold arise due to "underlying events", e.g. electrons or positrons with low momentum that do not fulfill the trigger conditions but are part of an event that was triggered by electrons or positrons that do fulfill the trigger conditions. The Monte Carlo simulation (for details see Section 3.3) reproduces the differences for electrons and positrons due to the ExB effect as well as the p_{T} threshold. However, the general slope behaviour for both charges does not match our results. Instead of reaching a plateau value for higher momenta, the determined trigger efficiency for Monte Carlo simulations slowly increases and asymptotically approaches a final value. Furthermore, the efficiency for lower momenta is significantly larger for the Monte Carlo simulated data. The differences are due to different particle abundances and p_{T}-distributions in MC simulations and physics data.

5.2 Comparison with the TRD trigger in p-Pb collisions

In this section, the TRD electron trigger efficiency is compared with the one in proton-lead collisions at $\sqrt{s} = 8.16$ TeV [14]. The conditions for the HQU trigger were exactly the same as for this thesis, except in this thesis, a PID cut value of 130 has been used instead of 135. Since the center-of-mass energy for this thesis is higher and the data taking was spread over two years, one expects more statistics to work with. Thus, one expects more precise results with smaller uncertainties than in [14]. One also expects to see the same trigger characteristics for the p_{T} threshold and the different behaviour for electrons and positrons. Figures 5.3 and 5.4 show the direct comparison between the fitted trigger efficiencies for both studies.

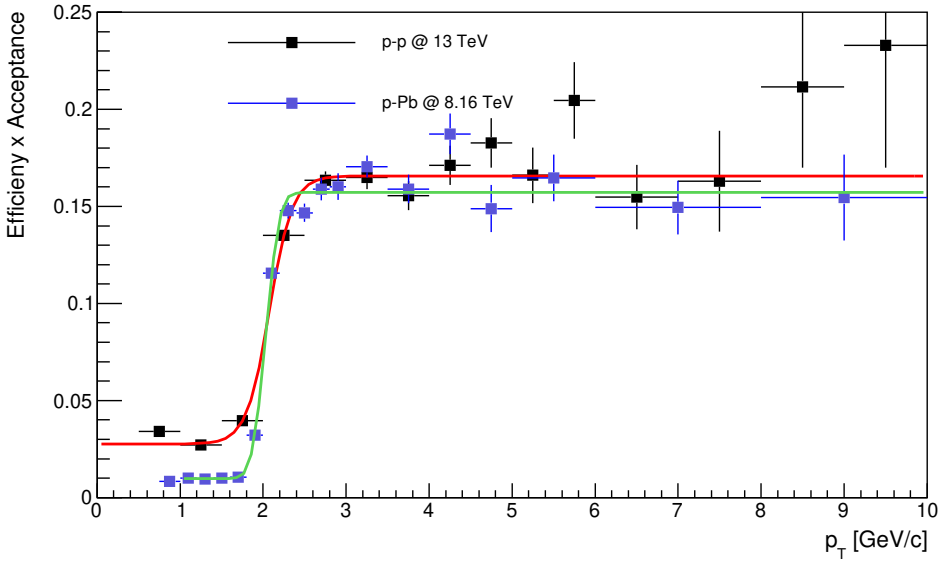

Figure 5.3: Fitted TRD trigger efficiencies for electrons. Shown are the fitted error functions for proton-proton collisions at $\sqrt{s} = 13$ TeV and proton-lead collisions at $\sqrt{s} = 8.16$ TeV. The shown errors are binomial errors.

The determined fitted electron efficiencies show the same expected characteristics. The p_{T}-threshold is visible as a sharp rise for electrons and for larger momenta, both efficiencies reach a constant value. However, the electron efficiency for $p_{\mathrm{T}} < 2\ \frac{\mathrm{GeV}}{c}$ is significantly larger for the proton-proton study.

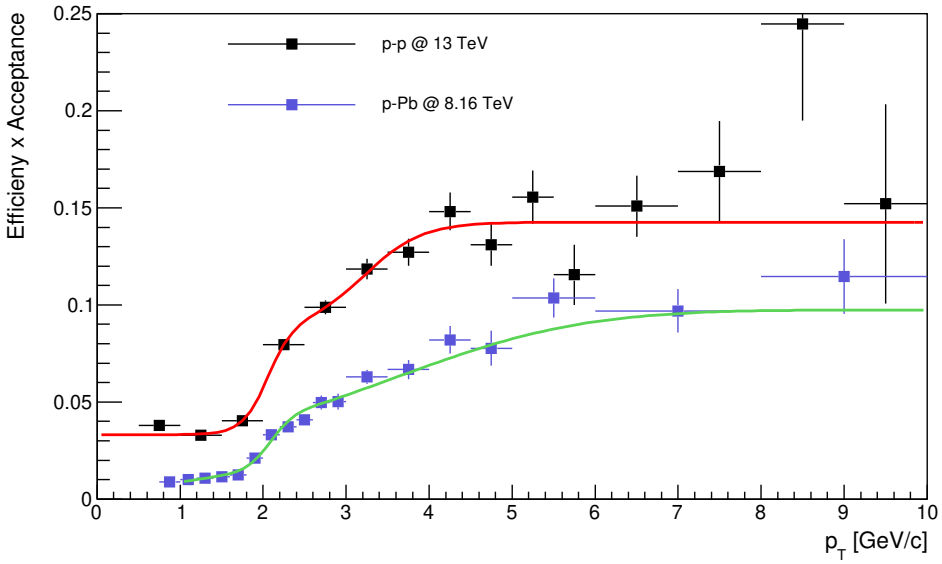

Figure 5.4: Fitted TRD trigger efficiencies for positrons. Shown are the fitted error functions for proton-proton collisions at $\sqrt{s} = 13$ TeV and proton-lead collisions at $\sqrt{s} = 8.16$ TeV. The shown errors are binomial errors.

Although the fitted positron efficiencies show the expected p_{T}-threshold characteristics, they deviate stronger from each other than the electron efficiencies. The plateau for the proton-proton collisions is noticeably higher than the plateau for proton-lead collisions. Furthermore, the slope of the second error function is different for the two studies. Again, the positron efficiency for $p_{\mathrm{T}} < 2\ \frac{\mathrm{GeV}}{c}$ is larger for the proton-proton study, which can also increase the efficiency plateau value. A further possible explanation for the larger differences in the positron efficiencies may be the used magnetic field settings. For the data taking periods in the year 2017, the magnet was operated at $B = -0.5T$ along the beam direction. However, from LHC18g onwards the polarity of the magnet was changed to $B = +0.5T$. Figure 5.5 shows the positron trigger efficiencies for the data taking periods LHC18f ($B = -0.5T$) and LHC18l ($B = +0.5T$).

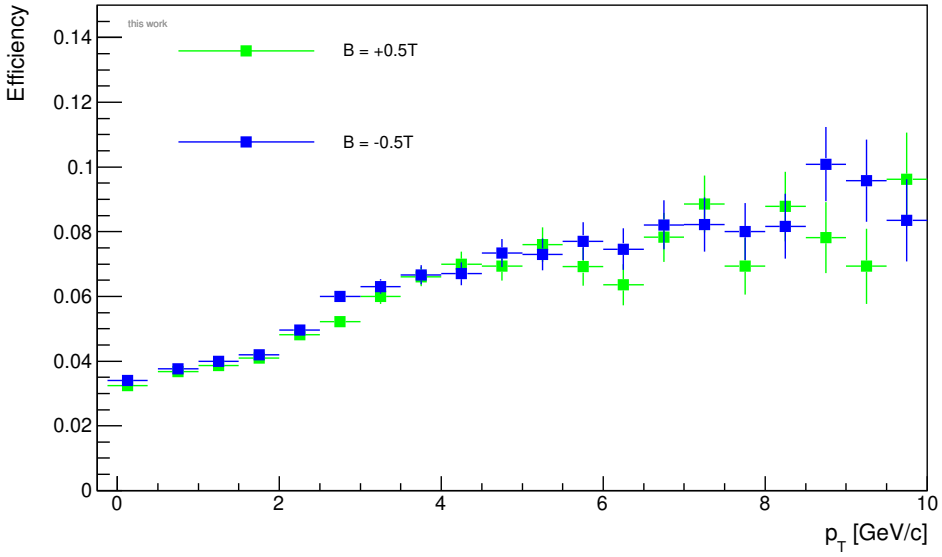

Figure 5.5: TRD trigger efficiency for positrons for the data taking periods LHC18f ($B = -0.5T$) and LHC18l ($B = +0.5T$) as a function of the transverse momentum. The shown errors are binomial errors.

The data taking periods have been chosen as such, that the Xe-CO_2 ratio is roughly the same. This enables us to check for possible differences arising due to the settings of the magnetic field. However, the shown efficiencies for the different polarities show no significant differences. Hence, one can conclude that the change in polarity of the magnetic field does not influence our results.

6 | Conclusion and Outlook

This thesis presents the ALICE TRD electron trigger performance for proton-proton collisions at $\sqrt{s} = 13$ TeV. Suitable electron candidates were identified using the TPC $n_{\sigma,e}$, which quantifies the deviation of the measured average energy loss of a particle from the theoretically predicted energy loss of an electron, given by the Bethe-Bloch equation, divided by the detector resolution. To reject hadrons, a hard cut has been applied to the TPC $n_{\sigma,e}$.

However, there are still hadron contributions for larger momenta. Therefore, a more technical approach has been used to remove the hadron contamination. One-dimensional projections were performed for each p_{T}-bin on the TPC $n_{\sigma,e}$ and the electron and hadron contributions were fitted using two gaussian distributions. The validity of usage of the gaussian fits could be verified with the help of electrons from photon conversion. The hadron contamination was then determined as the shared area of the two fit functions for a given range. The efficiency was then calculated as the ratio of the p_{T} spectrum of electrons which fulfill the TRD trigger conditions in the minimum bias sample to the one in the minimum bias sample. The calculated efficiencies show two distinct features. Firstly, the efficiencies show the expected sharp on-set at the p_{T} trigger threshold of $p_{\mathrm{T}} = 2\ \frac{\mathrm{GeV}}{c}$. Secondly, the positron trigger efficiency showed a less steep rise and was described better by two error functions instead of one. This was also expected due to the ExB effect. In order to reduce the amount of needed code, it was investigated if a hard PID hadron rejection and electron cut is sufficient for the efficiency determination. The found results agree well with the manual method described earlier.

Physics studies use TRD triggered data. One has to take this into account, since minimum bias data has been used up to this point. Furthermore, the efficiency of the ALICE TRD was found to be linearly dependent on the gain. To take this into account, a runwise efficiency was determined. The runs were sorted according to their gain into categories. Then, the spectra of the gain categories were summed up, using the number of TRD events per gain category as a weight. The final efficiency was again determined by calculating the ratio of minimum bias spectra that fulfill the TRD trigger conditions to the minimum bias spectra. The final efficiency showed the same expected characteristics due to the p_{T}-threshold and the ExB effect. For both charges, the final efficiency reaches a plateau value for $p_{\mathrm{T}} > 5\ \frac{\mathrm{GeV}}{c}$. For electrons, this plateau is already reached for $p_{\mathrm{T}} > 2.5\ \frac{\mathrm{GeV}}{c}$. For momenta up to $p_{\mathrm{T}} < 10\ \frac{\mathrm{GeV}}{c}$, one gets excellent results. For larger momenta, there are large uncertainties due to statistical fluctuations and a possibly remaining hadron contamination. Although the Monte Carlo simulation was able to reproduce the threshold behaviour and the ExB effect, it does not show the expected constant efficiency for larger momenta. For larger momenta, the efficiency determined with the Monte Carlo simulated data asymptotically approaches some final value. In general, the ALICE TRD performance in Monte Carlo simulations does not match the calculated performance for physics data. The differences are due to different particle abundances and p_{T}-distributions in MC simulations and physics data. For further investigations, these effects have to be corrected for.

The determined trigger efficiencies for electrons and positrons correspond well to the results of a previous study in proton-lead collisions in 2016 [14]. The expected characteristics, namely the visible onset due to the p_{T}-trigger-threshold and the ExB effect, are nicely reproduced. However, the efficiencies of the proton-proton study, especially the positron efficiency, exhibit a larger plateau value. This is mainly due to the larger amount of underlying events in the proton-proton collision study. These events cause a larger offset from zero which causes a shift in the efficiency plateau.

In order to study the stability of the trigger efficiency, the efficiency using physics data as a function of the data taking period has also been calculated. One finds that the used gas mixture of xenon and carbon dioxide plays a crucial role. If there is not enough xenon in the TRD, the gain and thus the trigger efficiency decreases.

Although this thesis delivers excellent results for the ALICE TRD electron trigger performance for momenta up to $p_{\mathrm{T}} < 10\ \frac{\mathrm{GeV}}{c}$, there are large uncertainties for higher momenta. These uncertainties arise due to insufficient statistics and a possibly remaining hadron contamination. To collect more statistics, one could adjust the electron selection criteria to $-2 < n_{\sigma,e} < 3$ and then use the electromagnetic caloriemeter for particle identification. Furthermore, one can use TRD triggered data as a cross check for the efficiency determination at large momenta, as described in [14]. One finds that the ratio of xenon and carbon dioxide influence the trigger performance. Thus, it is crucial to keep this ratio constant in future. Lastly, one has to improve the settings of the Monte Carlo simulations, such that it better matches our results.

A | Additional figures

This section shows supporting material on the trigger observables, the particle identification and the analysis strategy.

A.1 Trigger observables

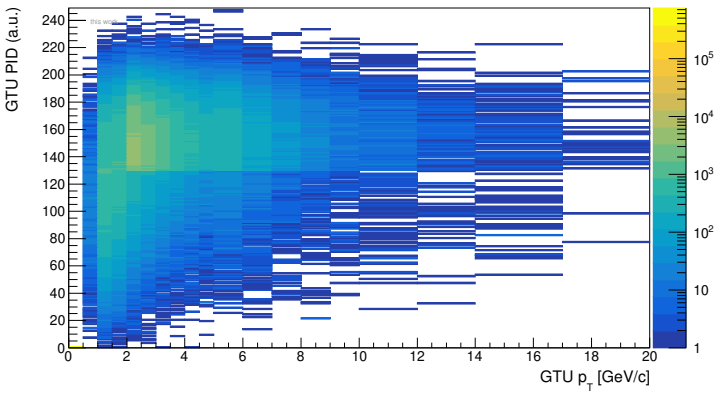

Figure A.1: Electron likelihood (GTU PID) as a function of the online reconstructed p_{T} for the TRD triggered physics sample.

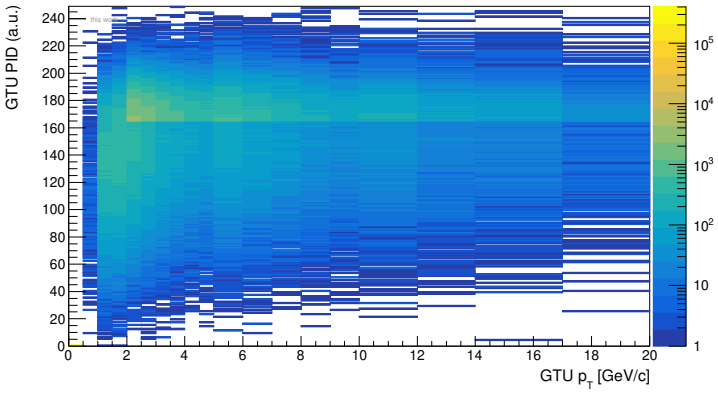

Figure A.2: Electron likelihood (GTU PID) as a function of the online reconstructed p_{T} for the Monte Carlo sample.

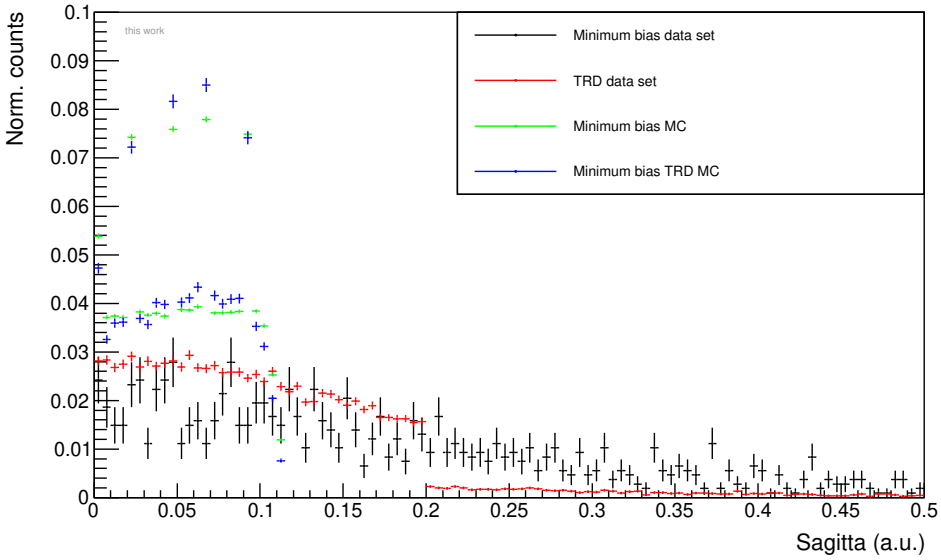

Figure A.3: Sagitta value for different data samples.

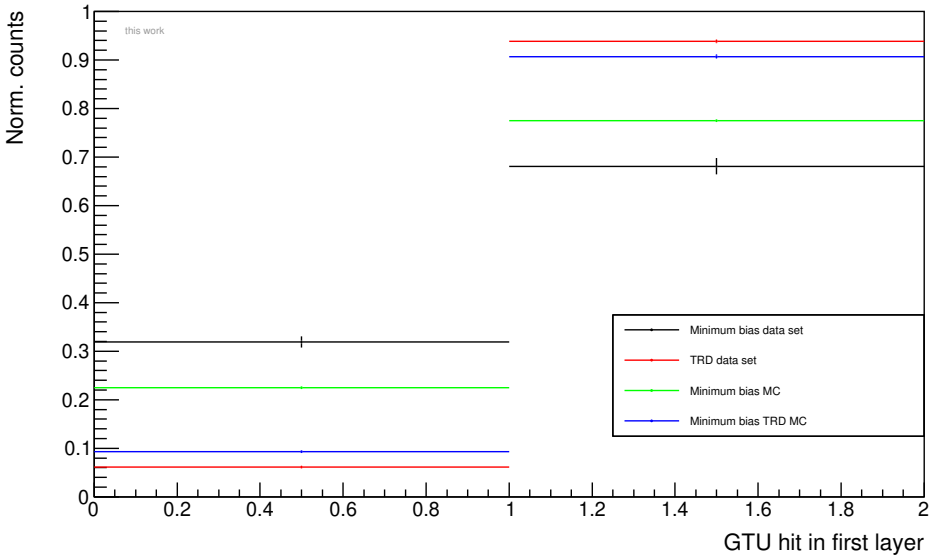

Figure A.4: First-layer-requirement for different data samples. The first bin (0-1) represents the case that the first layer has not been hit, the second bin (1-2) represents that the first layer has been hit.

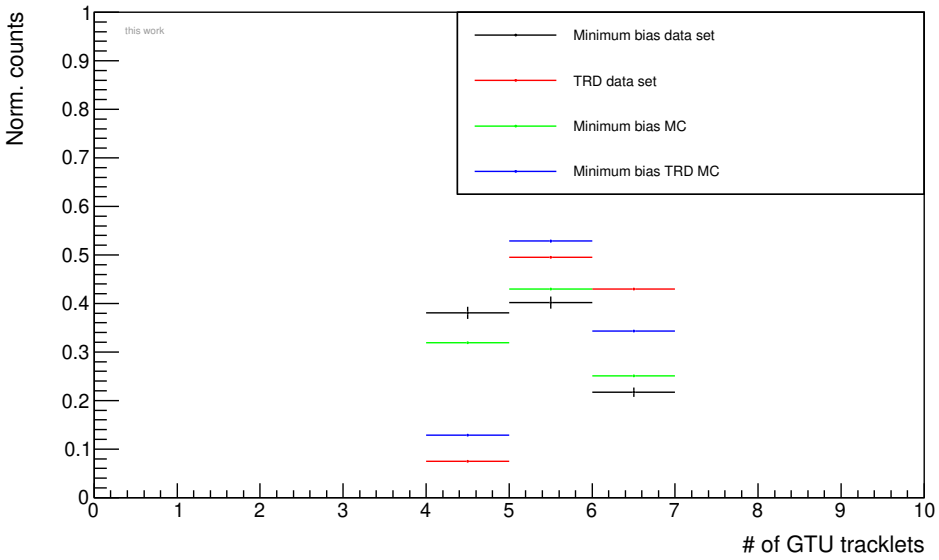

Figure A.5: Number of tracklets per track for different data samples.

A.2 Hadron rejection cut method

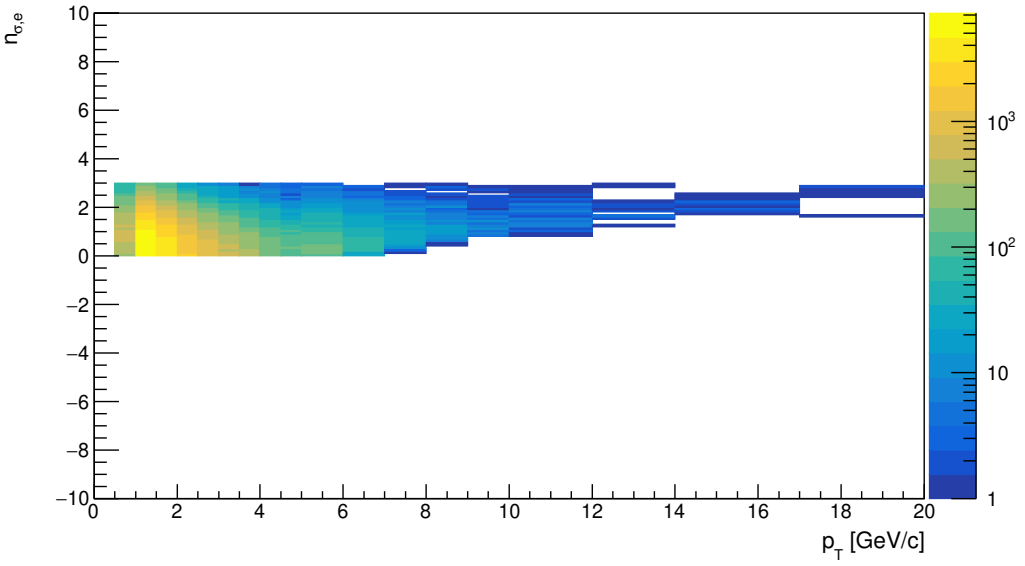

Figure A.6: TPC n_σ for the electron hypothesis with the applied selection criteria for electrons and rejection cuts for hadrons.

A.3 Hardware status of supermodules

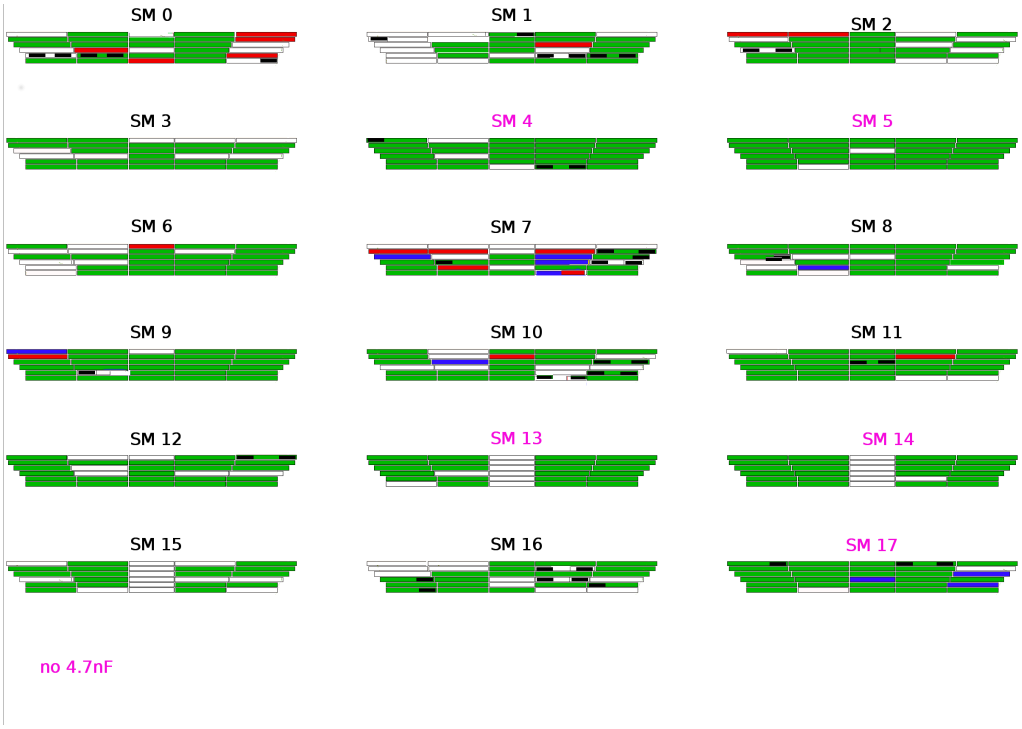

Figure A.7: ALICE TRD hardware status at the end of 2018. If chambers are marked as white, black or blue, they do not work. Green and red chambers are functional. The supermodules are numbered from zero to 17.

A.4 Runwise analysis

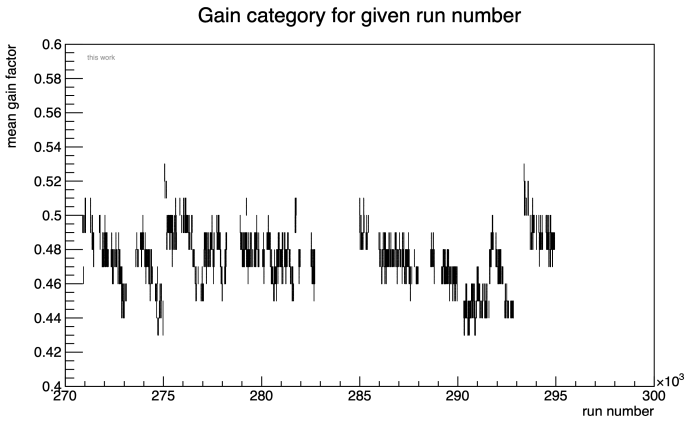

Figure A.8: Average chamber gain as a function of the run number. The mean gain is subdivided into 11 gain categories for analysis.

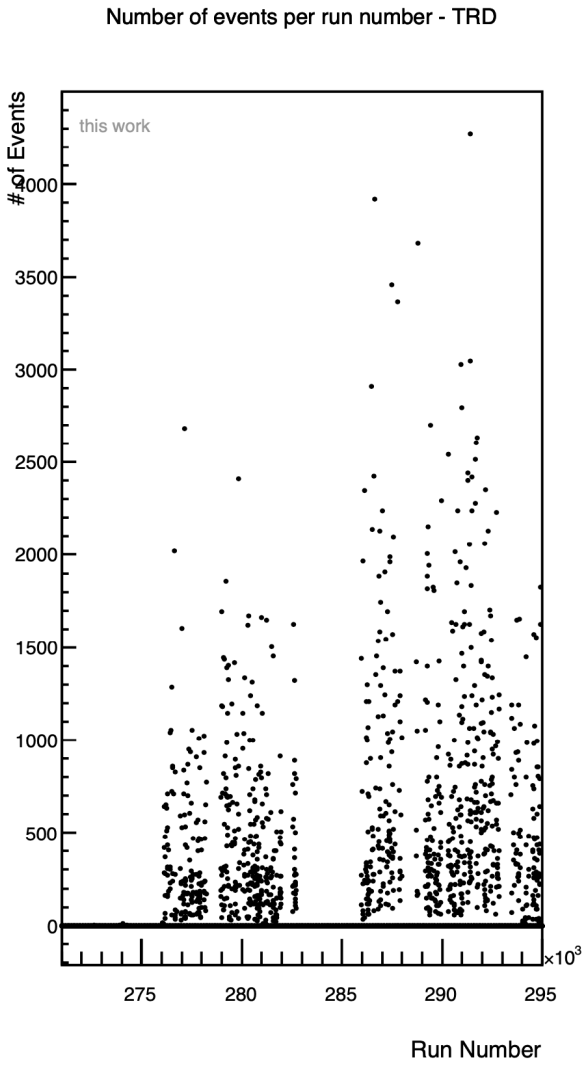

Figure A.9: Number of events as a function of the run number for the TRD triggered data sample.

A.5 Additional efficiency plots

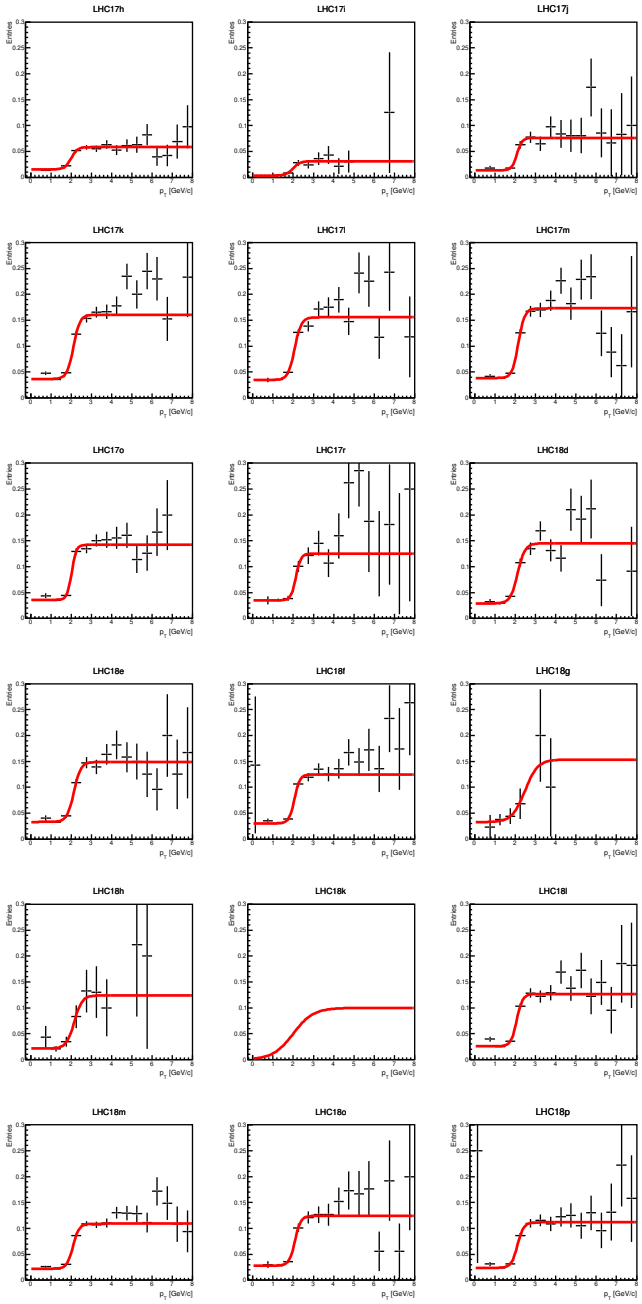

Figure A.10: Shown are the electron trigger efficiencies for each data taking period as a function of the transverse momentum for both charges combined. For each efficiency, an error function has been fitted (red line). The shown errors are binomial errors. For the data taking period LHC18k, there has been an unsolved problem with the run train code.

B | Runlist

LHC17h
271868, 271870, 271871, 271873, 271874, 271878, 271879, 271880, 271881, 271886, 271908, 271911, 271912, 271915, 271921, 271925, 271946, 271953, 271955, 271962, 271969, 271970, 272020, 272025, 272029, 272034, 272036, 272038, 272039, 272040, 272041, 272042, 272075, 272076, 272100, 272101, 272123, 272151, 272152, 272153, 272154, 272155, 272156, 272194, 272335, 272340, 272359, 272360, 272388, 272389, 272394, 272395, 272400, 272411, 272413, 272414, 272417, 272461, 272462, 272463, 272466, 272468, 272469, 272521, 272574, 272575, 272577, 272585, 272607, 272608, 272610, 272620, 272691, 272692, 272746, 272747, 272749, 272760, 272762, 272763, 272764, 272782, 272783, 272784, 272828, 272829, 272833, 272834, 272835, 272836, 272870, 272871, 272873, 272880, 272903, 272905, 272932, 272933, 272934, 272935, 272939, 272947, 272949, 272976, 272983, 272985, 273009, 273010, 273077, 273099, 273100, 273101, 273103

LHC17i
273824, 273825, 273885, 273886, 273887, 273889, 273918, 273942, 273946, 273985, 273986, 274058, 274063, 274064, 274092, 274094, 274125, 274147, 274148, 274212, 274232, 274259, 274263, 274264, 274266, 274268, 274269, 274270, 274271, 274276, 274278, 274280, 274281, 274283, 274329, 274352, 274355, 274357, 274360, 274363, 274364, 274442

LHC17j
274593, 274595, 274601, 274657, 274669, 274594, 274596, 274653, 274667, 274671

LHC17k
274736, 274801, 274802, 274803, 274806, 274807, 274811, 274815, 274817, 274822, 274877, 274878, 274882, 274883, 274884, 274886, 274978, 274979, 275067, 275068, 275075, 275076, 275150, 275151, 275173, 275174, 275177, 275180, 275184, 275188, 275239, 275245, 275246, 275247, 275283, 275314, 275322, 275324, 275326, 275328, 275332, 275333, 275360, 275361, 275369, 275372, 275394, 275395, 275401, 275406, 275443, 275453, 275456, 275457, 275459, 275467, 275472, 275515, 275558, 275559, 275612, 275621, 275622, 275623, 275624, 275647, 275648, 275650, 275657, 275661, 275847, 275924, 275925, 276012, 276013, 276017, 276040, 276041, 276045, 276098, 276099, 276102, 276104, 276105, 276108, 276135, 276140, 276141, 276145, 276166, 276169, 276170, 276177, 276178, 276230, 276259, 276290, 276291, 276292, 276294, 276297, 276302, 276307, 276312, 276348, 276351, 276429, 276435, 276437, 276438, 276439, 276462, 276506, 276507, 276508

LHC17l
276551, 276552, 276553, 276557, 276608, 276644, 276669, 276670, 276671, 276672, 276674, 276675, 276762, 276916, 276917, 276920, 276969, 276970, 276971, 276972, 277015, 277016,

277017, 277037, 277073, 277076, 277079, 277082, 277087, 277091, 277117, 277121, 277155, 277180, 277181, 277182, 277183, 277184, 277188, 277189, 277193, 277194, 277196, 277197, 277256, 277257, 277262, 277293, 277310, 277312, 277314, 277360, 277383, 277384, 277386, 277389, 277417, 277418, 277470, 277472, 277473, 277476, 277477, 277478, 277479, 277530, 277531, 277534, 277536, 277537, 277574, 277575, 277576, 277577, 277721, 277723, 277725, 277745, 277746, 277747, 277749, 277794, 277795, 277799, 277800, 277801, 277802, 277805, 277834, 277836, 277841, 277842, 277845, 277847, 277848, 277870, 277876, 277897, 277898, 277899, 277900, 277901, 277903, 277904, 277907, 277930, 277952, 277987, 277988, 277989, 277991, 277996, 278121, 278122, 278123, 278126, 278127, 278130, 278163, 278164, 278165, 278166, 278167, 278189, 278191, 278215, 278216

LHC17m

278959, 278960, 278963, 278964, 278999, 279000, 279005, 279007, 279008, 279035, 279036, 279041, 279043, 279044, 279068, 279069, 279073, 279074, 279075, 279106, 279107, 279117, 279118, 279122, 279123, 279130, 279155, 279157, 279199, 279201, 279207, 279208, 279234, 279235, 279238, 279242, 279264, 279265, 279267, 279268, 279270, 279273, 279274, 279309, 279310, 279312, 279342, 279344, 279348, 279349, 279354, 279355, 279391, 279410, 279435, 279439, 279441, 279483, 279487, 279488, 279491, 279550, 279559, 279630, 279632, 279641, 279642, 279676, 279677, 279679, 279682, 279683, 279684, 279688, 279689, 279715, 279718, 279719, 279747, 279749, 279773, 279826, 279827, 279830, 279853, 279854, 279855, 279879, 279880, 280051, 280052, 280066, 280107, 280108, 280111, 280114, 280118, 280126, 280131, 280134, 280135, 280140

LHC17o

280282, 280283, 280284, 280285, 280286, 280290, 280310, 280312, 280348, 280349, 280350, 280351, 280352, 280374, 280375, 280403, 280405, 280406, 280412, 280413, 280415, 280419, 280443, 280445, 280446, 280447, 280448, 280490, 280499, 280518, 280519, 280546, 280547, 280550, 280551, 280574, 280575, 280576, 280581, 280583, 280613, 280634, 280636, 280637, 280639, 280645, 280647, 280648, 280650, 280671, 280673, 280676, 280679, 280681, 280705, 280706, 280729, 280753, 280754, 280755, 280756, 280757, 280761, 280763, 280764, 280765, 280766, 280767, 280768, 280786, 280787, 280792, 280793, 280842, 280844, 280845, 280847, 280848, 280849, 280854, 280856, 280880, 280881, 280890, 280897, 280936, 280940, 280943, 280947, 280990, 280994, 280996, 280997, 280998, 280999, 281032, 281033, 281035, 281036, 281079, 281080, 281081, 281179, 281180, 281181, 281189, 281190, 281191, 281212, 281213, 281240, 281241, 281242, 281243, 281244, 281271, 281273, 281275, 281277, 281301, 281321, 281350, 281415, 281441, 281443, 281444, 281446, 281449, 281450, 281475, 281477, 281509, 281511, 281557, 281562, 281563, 281568, 281569, 281574, 281580, 281581, 281583, 281592, 281633, 281705, 281706, 281707, 281709, 281713, 281741, 281750, 281751, 281753, 281754, 281755, 281892, 281893, 281894, 281895, 281915, 281916, 281918, 281920, 281928, 281931, 281932, 281939, 281940, 281953, 281956, 281961

LHC17r

282528, 282544, 282545, 282546, 282573, 282575, 282579, 282580, 282606, 282607, 282608, 282609, 282618, 282620, 282622, 282629, 282651, 282653, 282666, 282667, 282668, 282670, 282671, 282673, 282676, 282677, 282700, 282702, 282703, 282704

LHC18d

285978, 285979, 285980, 286014, 286025, 286027, 286028, 286030, 286064, 286124, 286127, 286129, 286130, 286159, 286198, 286199, 286201, 286202, 286203, 286229, 286230, 286231, 286254, 286255, 286257, 286258, 286261, 286263, 286282, 286284, 286287, 286288, 286289,

286308, 286309, 286310, 286312, 286314, 286336, 286337, 286340, 286341, 286345, 286348, 286349, 286350

LHC18e

286380, 286426, 286427, 286428, 286454, 286455, 286501, 286502, 286508, 286509, 286566, 286567, 286568, 286569, 286591, 286592, 286594, 286653, 286661, 286695, 286731, 286799, 286801, 286805, 286809, 286810, 286846, 286848, 286850, 286852, 286874, 286876, 286877, 286907, 286908, 286910, 286911, 286930, 286931, 286932, 286933, 286936, 286937

LHC18f

287000, 287021, 287063, 287064, 287066, 287071, 287072, 287077, 287137, 287155, 287201, 287202, 287203, 287204, 287208, 287209, 287248, 287249, 287250, 287251, 287254, 287283, 287324, 287325, 287343, 287344, 287346, 287347, 287349, 287353, 287355, 287356, 287360, 287380, 287381, 287385, 287387, 287388, 287389, 287413, 287451, 287480, 287481, 287484, 287486, 287513, 287516, 287517, 287518, 287520, 287521, 287524, 287573, 287575, 287576, 287578, 287654, 287656, 287657, 287658, 287783, 287784, 287876, 287877, 287883, 287884, 287885, 287911, 287912, 287913, 287915, 287923, 287941, 287975, 287977

LHC18g

288687, 288689, 288690, 288743, 288748, 288750

LHC18h

288806

LHC18k

289165, 289166, 289167, 289169, 289172, 289176, 289177, 289198, 289199, 289200, 289201

LHC18l

289240, 289241, 289242, 289243, 289247, 289249, 289253, 289254, 289275, 289276, 289277, 289278, 289280, 289300, 289303, 289306, 289308, 289309, 289353, 289354, 289355, 289356, 289363, 289365, 289366, 289367, 289368, 289369, 289370, 289373, 289374, 289426, 289444, 289462, 289463, 289465, 289466, 289468, 289493, 289494, 289547, 289574, 289576, 289577, 289582, 289625, 289632, 289657, 289658, 289659, 289660, 289664, 289666, 289721, 289723, 289724, 289729, 289731, 289732, 289757, 289775, 289808, 289811, 289814, 289815, 289816, 289817, 289818, 289830, 289849, 289852, 289854, 289855, 289856, 289857, 289880, 289884, 289928, 289931, 289935, 289940, 289941, 289943, 289966, 289971

LHC18m

290293, 290294, 290297, 290298, 290300, 290323, 290324, 290327, 290350, 290374, 290375, 290401, 290404, 290411, 290412, 290423, 290425, 290427, 290428, 290456, 290458, 290459, 290467, 290469, 290499, 290501, 290538, 290539, 290540, 290544, 290549, 290550, 290553, 290590, 290612, 290613, 290614, 290615, 290627, 290632, 290645, 290658, 290660, 290665, 290687, 290692, 290696, 290699, 290721, 290742, 290764, 290766, 290769, 290774, 290776, 290787, 290790, 290841, 290846, 290848, 290853, 290860, 290862, 290886, 290887, 290888, 290892, 290894, 290895, 290932, 290935, 290941, 290943, 290944, 290948, 290974, 290975, 290976, 290979, 290980, 291002, 291003, 291004, 291005, 291006, 291035, 291037, 291041, 291065, 291066, 291093, 291100, 291101, 291110, 291111, 291116, 291143, 291209, 291240, 291257, 291263, 291265, 291266, 291282, 291283, 291284, 291285, 291286, 291360, 291361, 291362, 291363, 291373, 291375, 291377, 291397, 291399, 291400, 291402, 291416, 291417, 291419, 291420, 291424, 291446, 291447, 291451, 291453, 291456, 291457, 291481, 291482,

291484, 291485, 291590, 291614, 291615, 291618, 291622, 291624, 291626, 291657, 291661, 291665, 291690, 291692, 291694, 291697, 291698, 291702, 291706, 291729, 291755, 291756, 291760, 291762, 291766, 291768, 291769, 291795, 291796, 291803, 291942, 291943, 291944, 291945, 291946, 291948, 291953, 291976, 291977, 291982, 292012, 292040, 292060, 292061, 292062, 292067, 292075, 292077, 292080, 292081, 292106, 292107, 292108, 292109, 292114, 292115, 292140, 292160, 292161, 292162, 292163, 292164, 292166, 292167, 292168, 292192, 292240, 292241, 292242, 292265, 292269, 292270, 292273, 292274, 292298, 292397, 292398, 292405, 292406, 292428, 292429, 292430, 292432, 292434, 292456, 292457, 292460, 292461, 292495, 292496, 292497, 292500, 292521, 292523, 292524, 292526, 292553, 292554, 292557, 292559, 292560, 292563, 292584, 292586, 292693, 292695, 292696, 292698, 292701, 292704, 292737, 292739, 292744, 292747, 292748, 292752, 292754, 292758, 292803, 292804, 292809, 292810, 292811, 292831, 292832, 292834, 292836, 292839

LHC18o

293413, 293474, 293475, 293494, 293496, 293497, 293570, 293573, 293578, 293583, 293587, 293588, 293686, 293689, 293691, 293692, 293695, 293740, 293741, 293770, 293773, 293774, 293799, 293802, 293805, 293807, 293809, 293829, 293830, 293831, 293856, 293886, 293891, 293893, 293896, 293898

LHC18p

294009, 294010, 294011, 294012, 294013, 294131, 294152, 294154, 294155, 294156, 294199, 294200, 294201, 294205, 294208, 294210, 294212, 294241, 294242, 294305, 294307, 294308, 294310, 294524, 294525, 294526, 294527, 294529, 294530, 294531, 294553, 294556, 294558, 294563, 294586, 294587, 294588, 294590, 294591, 294593, 294632, 294633, 294634, 294636, 294653, 294703, 294710, 294715, 294716, 294718, 294721, 294722, 294741, 294742, 294743, 294744, 294745, 294746, 294747, 294749, 294769, 294772, 294774, 294775, 294805, 294809, 294813, 294815, 294816, 294817, 294818, 294852, 294875, 294877, 294880, 294883, 294884, 294916, 294925

Bibliography

[1] V. L. Ginzburg and I.M Frank. "Radiation of a Uniformly Moving Electron Due to Its Transition from One Medium to Another". In: *J. Phys. (USSR)* 9 (1945), pp. 88–127.

[2] Volker Lindenstruth and Jan De Cuveland. "ALICE TRD Global Tracking Unit (GTU) - EDR Documentation". In: (May 2004).

[3] The ALICE Collaboration et al. "The ALICE experiment at the CERN LHC". In: *Journal of Instrumentation* 3.08 (Aug. 2008), S08002–S08002. DOI: 10.1088/1748-0221/3/08/s08002. URL: https://doi.org/10.1088/1748-0221/3/08/s08002.

[4] *Fermilab's CDF observes Omega-sub-b baryon*. June 2009. URL: https://www.symmetrymagazine.org/breaking/2009/06/29/fermilabs-cdf-observes-omega-sub-b-baryon (visited on 06/28/2022).

[5] J. Alme et al. "The ALICE TPC, a large 3-dimensional tracking device with fast readout for ultra-high multiplicity events". In: *Nuclear Instruments and Methods in Physics Research Section A: Accelerators, Spectrometers, Detectors and Associated Equipment* 622.1 (2010), pp. 316–367. ISSN: 0168-9002. DOI: https://doi.org/10.1016/j.nima.2010.04.042. URL: https://www.sciencedirect.com/science/article/pii/S0168900210008910.

[6] D. Baumeier. "V0 Decays: Documentation of the C++ Program AliESDv0KineCuts.cxx". Bachelor's thesis. Universität Münster, 2011, pp. 5–9.

[7] M. Thomson. *Modern Particle Physics*. Cambridge University Press, 2013, pp. 1–29.

[8] The ALICE collaboration. "First results of the ALICE detector performance at 13 TeV". In: (Aug. 2015). URL: https://cds.cern.ch/record/2047855.

[9] Sunghoon Jung and Hye-Sung Lee. *Constraining Higgsino Kink Tracks from Existing LHC Searches*. 2015. DOI: 10.48550/ARXIV.1503.00414. URL: https://arxiv.org/abs/1503.00414.

[10] O. Schmidt. "Simulation and commissioning of the rejection of late conversions in the TRD triggers of ALICE". MA thesis. Universität Heidelberg, 2016, pp. 5–9.

[11] The ALICE Collaboration et al. "The ALICE Transition Radiation Detector: Construction, operation, and performance". In: *Nuclear Instruments and Methods in Physics Research Section A: Accelerators, Spectrometers, Detectors and Associated Equipment* 881 (Feb. 2018), pp. 88–127. DOI: 10.1016/j.nima.2017.09.028. URL: https://doi.org/10.1016%2Fj.nima.2017.09.028.

[12] *Standard Model of Elementary Particles*. July 2019. URL: https://en.wikipedia.org/wiki/File:Standard_Model_of_Elementary_Particles.svg (visited on 06/28/2022).

[13] Torbjörn Sjöstrand. "The Pythia event generator: Past, present and future". In: *Computer Physics Communications* 246 (Jan. 2020), p. 106910. DOI: 10.1016/j.cpc.2019.106910. URL: https://doi.org/10.1016%2Fj.cpc.2019.106910.

[14] Y. Pachmayer et al. “Measurement of J/Ψ in TRD-triggered p-Pb collisions at $\sqrt{s_{NN}}$ = 8.16 TeV with ALICE at the LHC”. ALICE Internal Analysis Note. 2021, pp. 12–16.

[15] Y. Pachmayer, private communication.

Erklärung

Ich versichere, dass ich diese Arbeit selbstständig verfasst und keine anderen als die angegebenen Quellen und Hilfsmittel benutzt habe.

Heidelberg, den 13.07.2021,

Felix Waldherr

Acknowledgements

This thesis would not have been possible without Priv. Doz. Dr. Yvonne Pachmayer. She is always kind, available if help is needed and also pushed me to critically think on my own. Therefore I extend my deepest gratitude. Furthermore, I want to thank Prof. Dr. Johanna Stachel for kindly accepting to be the second referee for this thesis.

I want to thank my parents and my brother for always being by my side, supporting me and making all of this possible. I want to thank Kim, Carlotta, Alex and Julian not only for proof-reading my thesis, but also for being great friends during the time of studies. In addition, I would like to thank Minjung Kim, Sophie Rohletter and the entire ALICE group for all the help I received. Also, I would like to thank my dear friend Linda, who is always there when I needed someone to chat, gossip or anything like that.

Last but not least, I wanna thank me
I wanna thank me for believing in me
I wanna thank me for doing all this work
I wanna thank me for, for never quitting
I wanna thank me for just being me at all times
- *Snoop Dogg*